Elastic P and S wave autofocus imaging with primaries and internal multiples

Elastic P and S wave autofocus imaging with primaries and internal multiples

Carlos Alberto da Costa Filho,* Matteo Ravasi* and Andrew Curtis*

* *University of Edinburgh,*

Grant Institute, James Hutton Road

King's Buildings,Edinburgh, UK, EH9 3FE

(May 26, 2015)

Running head: **Elastic autofocus imaging**

ABSTRACT

Conventional seismic imaging methods rely on the single-scattering Born approximation, requiring the removal of multiply scattered events from reflection data prior to imaging. Additionally, many methods use an acoustic approximation, representing the solid Earth as an acoustic (fluid) medium. We propose imaging methods for (solid) elastic media that use primaries and internal multiples, including their PS and SP conversions, thus obviating the need for internal multiple removal and improving handling of internal conversions. The methods rely on the elastic autofocusing method which creates multi-component elastodynamic Green's functions from virtual sources interior to the medium to receivers placed on the surface. They require only surface seismic reflection data and estimates of the direct waves from virtual sources interior to the medium, both of which are commonly available at the imaging step of seismic processing. We demonstrate our methods on a synthetic model with constant P and S velocities and vertical and horizontal density variations, by producing for the first time PP and SS images from elastic autofocusing which are compared to

reference seismic images based on conventional methods. Effects of multiples are greatly attenuated in the images, with fewer spurious reflectors than are observed when using Born imaging.

INTRODUCTION

Imaging the subsurface of the Earth is an important part of seismic exploration and monitoring. When using standard seismic data which always records multiply-scattered wavefields, two different approaches to seismic imaging are identified: those which use only primaries, and those which use both primaries and multiples to form the image. Conventional and commonly used methods such as Kirchoff migration (Schneider, 1978; Kuo and Dai, 1984; Bleistein, 1987), wave equation migration (Claerbout, 1971; Stoffa et al., 1990), reverse-time migration (RTM) (Baysal et al., 1983; Chang and McMechan, 1986, 1994) and least squares migration (Nemeth et al., 1999) assume all energy is singly scattered; the data used in these methods cannot contain multiply-scattered or multiply-reflected waves. Falling in the first category, these methods make use of multiple removal techniques as a common pre-imaging procedure.

Free-surface related multiples generate particularly strong spurious structures in images though their removal is generally straightforward, and various methods are available for marine pressure streamer data (Verschuur, 1991, 1992), ocean-bottom cable (OBC) and multicomponent marine steamer data (Ziolkowski et al., 1999; Amundsen, 2001; Majdański et al., 2011). The same is not true for internal multiples, which often require detailed subsurface information for their effective removal. Some methods require a model of the subsurface (Pica and Delmas, 2008), while others require manual identification of primaries (Jakubowicz, 1998). Data-driven methods for multiple prediction exist, but each has their own drawback. Inverse-scattering series based methods (Weglein et al., 1997) accurately estimates the kinematics of the multiples but, for their removal, requires knowledge of the seismic source wavelets which may either be recorded or estimated. The common-focus-

point (CFP) method (Berkhout and Verschuur, 2005), requires some manual interpretation of the data. Reshef et al. (2006) offers a method for estimating the kinematics of internal multiples that does not need prestack data, but is limited to hyperbolic moveouts. Ikelle (2006) also proposed a data-driven method for internal multiple attenuation, but which needs the user to select time windows containing primaries. Recently, another kind of data-driven method has been proposed which uses the method of autofocusing to predict multiples that must be adaptively subtracted (Meles et al., 2014). Autofocusing is at the foundation of the current paper and is explained below. In the above methods, adaptive filtering and subtraction must be used, and may harm primary energy content (Abma et al., 2005) or may not remove all multiple energy, and imperfect multiple removal often results in spurious structures in images which hamper their interpretation (Malcolm et al., 2007).

The second category of imaging methods comprises those which *use* multiply scattered wave energy to create the image, thus bypassing the need for multiple removal. One of the first such methods was proposed by Reiter et al. (1991) which used ray based Kirchhoff migration to migrate deep water multiples. Berkhout and Verschuur (2006) developed a model-independent method to image using any surface-related multiple. Youn and Zhou (2001) devised a prestack depth migration method that used a model-based estimate of the internal multiples. Data-driven methods for imaging using internal multiples include least squares migration (Brown and Guitton, 2005), interferometric imaging (Jiang et al., 2005), one-way wave equation migration (Malcolm et al., 2009), full wavefield migration (Berkhout, 2012), RTM for internal multiples (Liu et al., 2011; Fleury, 2013) and generalized internal multiple imaging (Zuberi and Alkhalifah, 2014).

A rather different class of imaging methods which utilize internal multiples have been developed recently. At the core of these methods is the autofocusing algorithm, a data-

driven method to estimate the response of a medium to up- or down-going sources at any of its internal points. These fields may be used directly for imaging using crosscorrelation or single-channel deconvolution based imaging conditions which is called autofocus imaging (Behura et al., 2014; Broggini et al., 2014a). So-called Marchenko imaging (Wapenaar et al., 2014), on the other hand, uses these fields to redatum the reflection data prior to performing a conventional imaging method such as RTM.

Rose (2001, 2002) first proposed the autofocusing method for 1D scattering media. He showed that it was possible to design incident wavefields that focus at one particular time at any chosen point interior to the medium (and only there); such focused fields then diverge similarly to waves from a subsurface source placed at a focusing location. Rose's method required that the scattered field from and to one side of the medium (the reflection response) be known, as well as the traveltime of a direct wave from the focus point to the same side of the medium. It was subsequently used in Broggini et al. (2012) for the construction of the Green's function resulting from a virtual source interior to an Earth-like medium, and extended to 3D scalar acoustic waves (Wapenaar et al., 2012, 2013). As opposed to one dimensional media where only the traveltime of the direct wave from the interior point to the exterior is needed, in the general 3D formulation the direct wavefield from the interior focus point to the surface is required. This can be estimated using a smooth, approximate macromodel of the subsurface velocity distribution, an estimate of which is commonly available at the imaging stage. The method also assumes that no free-surface multiples are present in the reflection response, an assumption that we maintain here but which is not an absolute requirement of the autofocusing method (Singh et al., 2014, 2015).

The above autofocusing-based methods are all only valid for acoustic (fluid) media. When used for seismic imaging, the Earth is therefore implicitly approximated by a fluid,

and hence solid effects such as shear waves and conversions are ignored. Autofocusing has recently been extended to elastic media using two different approaches. One approach uses P- and S-wave measured potentials from P- and S-wave potential sources (Wapenaar and Slob, 2014; Wapenaar, 2014) and another, velocity-stress recordings from force and deformation sources (da Costa et al., 2014a,b,c). Here we propose an elastic autofocus imaging method that correctly handles primaries and internal multiples, including converted-wave internal multiples, based on the latter method (da Costa et al., 2014a,b,c). Thus we extend autofocus imaging to solid media, which is more appropriate than its acoustic counterpart for real seismic field data, especially those arising from land or ocean bottom acquisitions.

We begin by introducing the necessary components of autofocusing theory using full velocity-stress data, and an approximation that uses only single-component velocity data. We then introduce a class of migration using conventional methods, and contrast that with autofocus imaging theory. By applying both methods to synthetic data we then compare their results for PP and SS imaging in a case where the true subsurface model is known exactly. Autofocusing based methods are shown to provide greatly reduced energy from spurious reflections and cross-talk, resulting in clearer, more interpretable images.

ELASTIC AUTOFOCUSING

In an isotropic elastic medium, with density $\rho(\mathbf{x})$ and stiffness tensor $c_{ijkl}(\mathbf{x})$, an elastodynamic wavefield with particle velocity $v_i(\mathbf{x},t)$ satisfies the following wave equation:

$$\partial_j c_{ijkl}(\mathbf{x})\partial_l v_k(\mathbf{x},t) - \partial_{tt}\rho(\mathbf{x})v_i(\mathbf{x},t) = s_{ij}(\mathbf{x},t) \tag{1}$$

Indices i,j,k and l may be x or y for the horizontal coordinates and z for the vertical coordinate, and Einstein notation is used meaning that there is an implicit summation over

all possible values of indices that are repeated within the same term. The source function can be written as

$$s_{ij}(\mathbf{x},t) = -\partial_t f_i(\mathbf{x},t) + \partial_j c_{ijkl}(\mathbf{x})\partial_l h_{kl}(\mathbf{x},t) \tag{2}$$

where $f_i(\mathbf{x},t)$ and $h_{kl}(\mathbf{x},t)$ represent external sources of volume force density and deformation rate density, respectively. We define Green's functions G as solutions to the wave equation in 1 from impulsive unidirectional force or deformation sources in equation 2, and denote them as $G^{(v,f)}_{(i,q)}(\mathbf{x},\mathbf{x}_0,t)$ or $G^{(v,h)}_{(i,pq)}(\mathbf{x},\mathbf{x}_0,t)$ respectively. The first and second Green's function superscripts represent the observed quantity and source type, while the two subscripts indicate the particular receiver and source components, respectively; its arguments, from left to right, are observation position, source position and time. For example, $G^{(v,f)}_{(i,q)}(\mathbf{x},\mathbf{x}_0,t)$ corresponds to the ith component of the particle velocity measured at $\mathbf{x}$ from an impulsive force source at $\mathbf{x}_0$ in the q direction. Moreover, stress Green's functions $G^{(\tau,\cdot)}_{(ij,\cdot)}(\mathbf{x},\mathbf{x}_0,t)$ can be defined from the velocity Green's functions using the generalized Hooke's law (Chapman, 2004):

$$\partial_t G^{(\tau,\cdot)}_{(ij,\cdot)} = c_{ijkl}\partial_l G^{(v,\cdot)}_{(k,\cdot)} \tag{3}$$

Finally, we will also consider receiving (emitting) P, SV or SH potentials. These can be obtained from the aforementioned Green's functions by applying to them the appropriate elastic wavefield decomposition differential operators described in Wapenaar and Haimé (1990), as long as the region around the receiver (source) is isotropic. They will be denoted by receiver (source) type ϕ with component N, where the latter can take values P, SV or SH. For example, the P potential may be obtained by applying the differential operator $(i\omega)^{-1}\rho c_P^2 \operatorname{div}(\cdot)$ in the angular frequency domain, where c_P is the velocity of the P-wave and $\operatorname{div}(\cdot)$ is the divergence of a vector field.

The purpose of elastic autofocusing is to estimate at the surface those Green's functions which have sources at points interior to the medium and receivers at the surface. Conversely, by reciprocity (Wapenaar and Fokkema, 2006) it also provides the Green's functions from surface sources measured at subsurface virtual receivers. Consider a point $\mathbf{x}_F$ in the subsurface, and points $\mathbf{x}_0$ and $\mathbf{x}_0'$ on the surface $\partial\mathbb{D}_0$, according to Figure 1. In order to derive a method for recovering the Green's functions from points $\mathbf{x}_0$ and $\mathbf{x}_0'$ to $\mathbf{x}_F$, we rely on a representation theorem given in da Costa et al. (2014a), which relates that Green's functions to so-called focusing functions. These focusing functions are solutions of the elastodynamic wave equation defined in a reference medium which is reflection-free above $\mathbf{x}_0$ and below $\mathbf{x}_F$. Their name stems from their property of focusing at a specific location at zero-time (see Appendix A). We use one type of focusing function in a version of the representation theorem of da Costa et al. (2014a) that states that the receiver-side N-wave potential of a Green's function measured at $\mathbf{x}_F$ from a force source at $\mathbf{x}_0'$ can be expressed in terms of a focusing functions $\underline{\mathbf{H}}$ and the up-going fields $\underline{\mathbf{G}}^-$ at the surface:

$$\underline{\mathbf{G}}_{(N)}^{(\phi)}(\mathbf{x}_F,\mathbf{x}_0',t)=\underline{\mathbf{H}}_{(N)}^{(\phi)}(\mathbf{x}_F,\mathbf{x}_0',-t)+\int_{\partial\mathbb{D}_0}\int_{-\infty}^{\infty}\underline{\mathbf{G}}^{-}(\mathbf{x}_0',\mathbf{x}_0,t-\tau)\,\underline{\mathbf{H}}_{(N)}^{(\phi)}(\mathbf{x}_F,\mathbf{x}_0,\tau)\,\mathrm{d}\tau\,\mathrm{d}^2\mathbf{x}_0 \quad (4)$$

where

$$\underline{\mathbf{G}}_{(N)}^{(\phi)}=\left(G_{(N,x)}^{(\phi,f)}\;\;G_{(N,y)}^{(\phi,f)}\;\;G_{(N,z)}^{(\phi,f)}\;\;G_{(N,xz)}^{(\phi,h)}\;\;G_{(N,yz)}^{(\phi,h)}\;\;G_{(N,zz)}^{(\phi,h)}\right)^T \quad (5)$$

$$\underline{\mathbf{H}}_{(N)}^{(\phi)}=\left(H_{(N,x)}^{(\phi,f)}\;H_{(N,y)}^{(\phi,f)}\;H_{(N,z)}^{(\phi,f)}\;-H_{(N,xz)}^{(\phi,h)}\;-H_{(N,yz)}^{(\phi,h)}\;-H_{(N,zz)}^{(\phi,h)}\right)^T \quad (6)$$

and

$$\underline{\mathbf{G}}^{-} = \begin{bmatrix} G^{-(v,h)}_{(x,xz)} & G^{-(v,h)}_{(x,yz)} & G^{-(v,h)}_{(x,zz)} & G^{-(v,f)}_{(x,x)} & G^{-(v,f)}_{(x,y)} & G^{-(v,f)}_{(x,z)} \\ G^{-(v,h)}_{(y,xz)} & G^{-(v,h)}_{(y,yz)} & G^{-(v,h)}_{(y,zz)} & G^{-(v,f)}_{(y,x)} & G^{-(v,f)}_{(y,y)} & G^{-(v,f)}_{(y,z)} \\ G^{-(v,h)}_{(z,xz)} & G^{-(v,h)}_{(z,yz)} & G^{-(v,h)}_{(z,zz)} & G^{-(v,f)}_{(z,x)} & G^{-(v,f)}_{(z,y)} & G^{-(v,f)}_{(z,z)} \\ G^{-(\tau,h)}_{(xz,xz)} & G^{-(\tau,h)}_{(xz,yz)} & G^{-(\tau,h)}_{(xz,zz)} & G^{-(\tau,f)}_{(xz,x)} & G^{-(\tau,f)}_{(xz,y)} & G^{-(\tau,f)}_{(xz,z)} \\ G^{-(\tau,h)}_{(yz,xz)} & G^{-(\tau,h)}_{(yz,yz)} & G^{-(\tau,h)}_{(yz,zz)} & G^{-(\tau,f)}_{(yz,x)} & G^{-(\tau,f)}_{(yz,y)} & G^{-(\tau,f)}_{(yz,z)} \\ G^{-(\tau,h)}_{(zz,xz)} & G^{-(\tau,h)}_{(zz,yz)} & G^{-(\tau,h)}_{(zz,zz)} & G^{-(\tau,f)}_{(zz,x)} & G^{-(\tau,f)}_{(zz,y)} & G^{-(\tau,f)}_{(zz,z)} \end{bmatrix} \tag{7}$$

[Figure 1 about here.]

This theorem relates the one-sided reflection response of the medium $\underline{\mathbf{G}}^{-}$, to the medium response $\underline{\mathbf{G}}^{(\phi)}_{(N)}$ measured at point $\mathbf{x}_F$ in the subsurface from sources on the surface. However, the focusing function $\underline{\mathbf{H}}^{(\phi)}_{(N)}$ is initially unknown; elastic autofocusing prescribes a way to construct it by iteration. First, adopt the *ansatz* (or model) for the sought focusing function

$$\underline{\mathbf{H}}^{(\phi)}_{(N)}(\mathbf{x}_F, \mathbf{x}_0, t) = \underline{\mathbf{G}}^{0(\phi)}_{(N)}(\mathbf{x}_F, \mathbf{x}_0, -t) + \theta(t + t^0_{(N)}(\mathbf{x}_F, \mathbf{x}_0))\, \underline{\mathbf{M}}^{(\phi)}_{(N)}(\mathbf{x}_F, \mathbf{x}_0, t) \tag{8}$$

where $\underline{\mathbf{G}}^{0(\phi)}_{(N)}(\mathbf{x}_F, \mathbf{x}_0, t)$ is the direct (non-scattered, non-converted, first arriving) N-wave from $\mathbf{x}_F$ to $\mathbf{x}_0$, $t^0_{(N)}(\mathbf{x}_F, \mathbf{x}_0)$ is its traveltime, θ is the Heaviside step function, and $\underline{\mathbf{M}}^{(\phi)}_{(N)}$ is a scattered coda. While the inclusion of $\underline{\mathbf{G}}^{0(\phi)}_{(N)}(\mathbf{x}_F, \mathbf{x}_0, -t)$ mirrors that in time-reversal approaches to wavefield focusing, the inclusion of $\underline{\mathbf{M}}^{(\phi)}_{(N)}(\mathbf{x}_F, \mathbf{x}_0, t)$ is essential for the cancellation of events that are introduced when propagating the time-reversed direct wavefield through the medium. An extensive analysis of these cancellations may be found in Wapenaar et al. (2014) for 2D acoustic media, and in Wapenaar (2014) for 2D horizontally layered elastic media.

According to the analysis in Appendix A, $\underline{\mathbf{H}}^{(\phi)}_{(N)}$ should be the inverse of the transmission

operator. This means that instead of using only the direct (non-scattered, non-converted, first arriving) N-wave followed by a scattered coda, a better estimate would include also forward-scattered converted events. This would also alter the window θ imposed on $\underline{\mathbf{M}}^{(\phi)}_{(N)}$ which would have to mute before the first-arriving event, be it converted or non-converted. Wapenaar (2014) analyses how the lack of these converted events hinders the quality of the focus and its associated Green's function retrieval. Wapenaar and Slob (2015) show that using the exact inverse of the transmission (including conversions) and the appropriate windows provides an exact reconstruction of the Green's functions in 2D layered isotropic elastic media, while omitting conversions causes artifacts. However, due to the difficulty of estimating the conversions without a detailed model of the reflectivity (which we lack prior to imaging), and the fact that most of the transmitted energy is contained in the non-converted event, we neglect converted arrivals.

Inserting this *ansatz* into the representation theorem in equation 4, evaluating the result for times before $t^0_{(N)}(\mathbf{x}_F, \mathbf{x}'_0)$, and neglecting converted waves that might arrive before the direct wave, all components on the left hand side equal zero, and we obtain a 3D vector-valued elastodynamic Marchenko equation:

$$\begin{aligned}\mathbf{0} = &\int_{\partial\mathbb{D}_0}\int_{-\infty}^{\infty} \underline{\mathbf{G}}^{-}(\mathbf{x}'_0, \mathbf{x}_0, t-\tau)\underline{\mathbf{G}}^{0(\phi)}_{(N)}(\mathbf{x}_F, \mathbf{x}_0, -\tau)\,\mathrm{d}\tau\,\mathrm{d}^2\mathbf{x}_0 \\ &+ \int_{\partial\mathbb{D}_0}\int_{-t^0_{(N)}}^{\infty} \underline{\mathbf{G}}^{-}(\mathbf{x}'_0, \mathbf{x}_0, t-\tau)\underline{\mathbf{M}}^{(\phi)}_{(N)}(\mathbf{x}_F, \mathbf{x}_0, \tau)\,\mathrm{d}\tau\,\mathrm{d}^2\mathbf{x}_0 + \underline{\mathbf{M}}^{(\phi)}_{(N)}(\mathbf{x}_F, \mathbf{x}'_0, -t) \end{aligned} \tag{9}$$

This equation can be solved by a two-step iteration: initialize a wavefield $\underline{\mathbf{P}}^{-}_{-1}(\mathbf{x}_F, \mathbf{x}_0, t) = \mathbf{0}$ and for $k \geq 0$ set

$$\underline{\mathbf{P}}^{+}_{k}(\mathbf{x}_F, \mathbf{x}_0, t) = \underline{\mathbf{G}}^{0(\phi)}_{(N)}(\mathbf{x}_F, \mathbf{x}_0, -t) - \theta(t + t^0_{(N)}(\mathbf{x}_F, \mathbf{x}_0))\underline{\mathbf{P}}^{-}_{k-1}(\mathbf{x}_F, \mathbf{x}_0, -t) \tag{10}$$

$$\underline{\mathbf{P}}^{-}_{k}(\mathbf{x}_F, \mathbf{x}'_0, t) = \int_{\partial\mathbb{D}_0}\int_{-\infty}^{\infty} \underline{\mathbf{G}}^{-}(\mathbf{x}'_0, \mathbf{x}_0, t-\tau)\underline{\mathbf{P}}^{+}_{k}(\mathbf{x}_F, \mathbf{x}_0, \tau)\,\mathrm{d}\tau\,\mathrm{d}\mathbf{x}_0 \tag{11}$$

It can be shown (da Costa et al., 2014a) that if the iteration converges, $\underline{\mathbf{P}}_k^-(\mathbf{x}_F, \mathbf{x}_0, t) = -\underline{\mathbf{M}}_{(N)}^{(\phi)}(\mathbf{x}_F, \mathbf{x}_0, -t)$, and consequently, from the representation theorem of equation 4,

$$\underline{\mathbf{G}}_{(N)}^{(\phi)}(\mathbf{x}_F, \mathbf{x}_0, t) = \underline{\mathbf{P}}^+(\mathbf{x}_F, \mathbf{x}_0, -t) + \underline{\mathbf{P}}^-(\mathbf{x}_F, \mathbf{x}_0, t) \tag{12}$$

where we use $\underline{\mathbf{P}}^+$ and $\underline{\mathbf{P}}^-$ for $\underline{\mathbf{P}}_k^+$ and $\underline{\mathbf{P}}_k^-$ respectively at the final iteration k of equations 10 and 11.

Provided that no evanescent waves exist at the subsurface virtual receiver location, $\underline{\mathbf{G}}_{(N)}^{(\phi)}$ can also be expressed in terms of up- and down-going fields; that is, $\underline{\mathbf{G}}_{(N)}^{(\phi)} = \underline{\mathbf{G}}_{(N)}^{-(\phi)} + \underline{\mathbf{G}}_{(N)}^{+(\phi)}$, where the $-/+$ superscripts indicate respectively the up- and down-going components at the receiver location. Therefore, the quantity ultimately recovered from the iteration on the left of equation 12 is the sum of the up- and down-going parts of the Green's function (where up- and down-going refers to the direction of travel of waves measured at the subsurface location). As shown in Appendix B, a similar iteration can be obtained to recover the *difference* between down- and upgoing fields (see Broggini et al. (2014b) for a detailed discussion on the layered acoustic case). That is, by initializing $\underline{\mathbf{Q}}_{-1}^-(\mathbf{x}_F, \mathbf{x}_0, t) = \mathbf{0}$, and for $k \geq 0$ set

$$\underline{\mathbf{Q}}_k^+(\mathbf{x}_F, \mathbf{x}_0, t) = \underline{\mathbf{G}}_{(N)}^{0(\phi)}(\mathbf{x}_F, \mathbf{x}_0, -t) + \theta(t + t_{(N)}^0(\mathbf{x}_F, \mathbf{x}_0))\underline{\mathbf{Q}}_{k-1}^-(\mathbf{x}_F, \mathbf{x}_0, -t) \tag{13}$$

$$\underline{\mathbf{Q}}_k^-(\mathbf{x}_F, \mathbf{x}_0', t) = \int_{\partial\mathbb{D}_0} \int_{-\infty}^{\infty} \underline{\mathbf{G}}^-(\mathbf{x}_0', \mathbf{x}_0, t-\tau)\underline{\mathbf{Q}}_k^+(\mathbf{x}_F, \mathbf{x}_0, \tau)\, \mathrm{d}\tau\, \mathrm{d}\mathbf{x}_0 \tag{14}$$

at convergence we obtain

$$\underline{\mathbf{G}}_{(N)}^{+(\phi)}(\mathbf{x}_F, \mathbf{x}_0, t) - \underline{\mathbf{G}}_{(N)}^{-(\phi)}(\mathbf{x}_F, \mathbf{x}_0, t) = \underline{\mathbf{Q}}^+(\mathbf{x}_F, \mathbf{x}_0, -t) + \underline{\mathbf{Q}}^-(\mathbf{x}_F, \mathbf{x}_0, t) \tag{15}$$

This means that by performing two separate but similar autofocusing schemes, one obtains up- and down-going Green's functions at the subsurface location without having to

perform an explicit wavefield decomposition:

$$2\underline{\mathbf{G}}^{+(\phi)}_{(N)}(\mathbf{x}_F,\mathbf{x}_0,t)=\underline{\mathbf{P}}^{+}(\mathbf{x}_F,\mathbf{x}_0,-t)+\underline{\mathbf{P}}^{-}(\mathbf{x}_F,\mathbf{x}_0,t)+\underline{\mathbf{Q}}^{+}(\mathbf{x}_F,\mathbf{x}_0,-t)+\underline{\mathbf{Q}}^{-}(\mathbf{x}_F,\mathbf{x}_0,t) \quad (16)$$

$$2\underline{\mathbf{G}}^{-(\phi)}_{(N)}(\mathbf{x}_F,\mathbf{x}_0,t)=\underline{\mathbf{P}}^{+}(\mathbf{x}_F,\mathbf{x}_0,-t)+\underline{\mathbf{P}}^{-}(\mathbf{x}_F,\mathbf{x}_0,t)-\underline{\mathbf{Q}}^{+}(\mathbf{x}_F,\mathbf{x}_0,-t)-\underline{\mathbf{Q}}^{-}(\mathbf{x}_F,\mathbf{x}_0,t). \quad (17)$$

However, since our *ansatz* of the focusing function does not include converted events, this reconstruction may have spurious arrivals as well as incorrect amplitudes of the recovered events (Wapenaar and Slob, 2015). Evanescent fields are also absent from the focusing function as these are not constructed by the above iteration.

SINGLE-COMPONENT ELASTIC AUTOFOCUSING

In order to perform the fully tensorial elastic autofocusing as shown in the previous section, one requires not only velocity measurements and force sources, but also stress measurements and deformation sources, which current acquisition technologies cannot provide. Provided that the medium satisfies some assumptions of homogeneity at the surface datum where autofocusing is performed, this requirement may be relaxed and the scheme may only require velocity from force sources. Recent work (Wapenaar and Slob, 2014; Wapenaar, 2014) uses this to recover Green's function P- and S-wave potentials from potential sources. Here we consider a simplification that assumes the waves travel mostly in the vertical direction (see Appendix C) and following da Costa et al. (2014b) propose a single-component approximation to the fully tensorial version of elastic autofocusing. In this formulation, only one component of the measured velocity is used, from a single unidirectional force source, allowing elastic autofocusing to be applied to OBC or multicomponent marine streamer data. For P-wave autofocusing, we use the vertical velocity measurements of the up-going scattered field at the surface from vertical force sources also at the surface, $G^{-(v,f)}_{(z,z)}(\mathbf{x}'_0,\mathbf{x}_0,t)$,

when attempting to recover the P-wave potential at subsurface location $\mathbf{x}_F$ from vertical surface force sources, $G^{(\phi,f)}_{(P,z)}(\mathbf{x}_F,\mathbf{x}_0,t)$ — or vice versa by source-receiver reciprocity (Wapenaar and Fokkema, 2006). In Appendix C we show that the use of only these components is obtained as a far-field approximation to elastic autofocusing when the medium around the sources $\mathbf{x}_0$ is isotropic with negligible shear strength. We thus derive a Marchenko equation which can be solved by the following autofocusing iteration on scalar p that is analogous to equations 10 and 11 which define tensorial $\underline{\mathbf{P}}$ autofocusing:

$$p^+_k(\mathbf{x}_F,\mathbf{x}_0,t) = G^{0(\phi,f)}_{(P,z)}(\mathbf{x}_F,\mathbf{x}_0,-t) - \theta(t+t^0_{(P)}(\mathbf{x}_F,\mathbf{x}_0))p^-_{k-1}(\mathbf{x}_F,\mathbf{x}_0,-t) \tag{18}$$

$$p^-_k(\mathbf{x}_F,\mathbf{x}'_0,t) = \int_{\partial\mathbb{D}_0}\int_{-\infty}^{\infty} G^{-(v,f)}_{(z,z)}(\mathbf{x}'_0,\mathbf{x}_0,t-\tau)p^+_k(\mathbf{x}_F,\mathbf{x}_0,\tau)\,\mathrm{d}\tau\,\mathrm{d}\mathbf{x}_0 \tag{19}$$

for $k \geq 0$ with $p^-_{-1} = 0$. An iteration equivalent to equations 13 and 14 for the analogous single-component approximation to $\underline{\mathbf{Q}}$ autofocusing (here referred to as q autofocusing) is obtained by summing, instead of subtracting, the second term on the right-hand side of equation 18:

$$q^+_k(\mathbf{x}_F,\mathbf{x}_0,t) = G^{0(\phi,f)}_{(P,z)}(\mathbf{x}_F,\mathbf{x}_0,-t) + \theta(t+t^0_{(P)}(\mathbf{x}_F,\mathbf{x}_0))q^-_{k-1}(\mathbf{x}_F,\mathbf{x}_0,-t) \tag{20}$$

$$q^-_k(\mathbf{x}_F,\mathbf{x}'_0,t) = \int_{\partial\mathbb{D}_0}\int_{-\infty}^{\infty} G^{-(v,f)}_{(z,z)}(\mathbf{x}'_0,\mathbf{x}_0,t-\tau)q^+_k(\mathbf{x}_F,\mathbf{x}_0,\tau)\,\mathrm{d}\tau\,\mathrm{d}\mathbf{x}_0 \tag{21}$$

One may then recover the up- and down-going Green's functions with

$$2G^{\pm(\phi,f)}_{(P,z)}(\mathbf{x}_F,\mathbf{x}_0,t) = p^+(\mathbf{x}_F,\mathbf{x}_0,-t) + p^-(\mathbf{x}_F,\mathbf{x}_0,t) \pm q^+(\mathbf{x}_F,\mathbf{x}_0,-t) \pm q^-(\mathbf{x}_F,\mathbf{x}_0,t) \tag{22}$$

where we drop the index k from $p^\pm$ and $q^\pm$ on the last iteration.

S-wave potentials in isotropic media obey the same scalar wave-equation as P-waves apart from variability in their seismic velocities (Chapman, 2004). We therefore introduce a similar single-component S-wave autofocusing with the same iterations as above, but

instead of using vertical velocity measurements and vertical force sources we use horizontal velocity measurements from horizontal force sources. Therefore the expression for S-wave autofocusing is obtained from equations 18, 19, 20 and 21 by substituting z indices for x indices and P potentials for S.

It is relevant to note that while the autofocusing algorithm used to estimate the wavefields in this approach are identical to the acoustic autofocusing of Broggini et al. (2012) and Wapenaar et al. (2013) which is entirely based on acoustic theory and hence fluid media, our approach is based on an approximation of the elastic tensorial autofocusing, and utilizes data containing P- and S-waves obtained from a solid subsurface medium. While in the single-component approximation in Appendix C the medium was approximated to be isotropic and shearless around the source locations $\mathbf{x}_0$, no restrictions are imposed on its attributes elsewhere. Thus the full theory and single-component approximations account for reflections and conversions between $\mathbf{x}_F$ and the surface and da Costa et al. (2014a,b) show that this even holds to a good approximation when applied in practice if the medium does not satisfy the condition of being shearless around the subsurface sources.

ELASTIC IMAGING

Claerbout (1971) identified that at points in the subsurface where there are reflectors, the first arrival of the down-going wave from a subsurface source coincides in time and space with the up-going wave resulting from its reflection (since the former creates the latter). In elastic media, relations between up-and down-going potentials and a certain subsurface point $\mathbf{x}_F$ have been formalized in several similar ways (Holvik and Amundsen, 2005; Wapenaar

et al., 2008; van der Neut et al., 2011). In the latter we find the expression

$$G^{-(\phi,\phi)}_{(M,K)}(\mathbf{x}_F,\mathbf{x}_0,\omega) = \int\limits_{\partial\mathbb{D}_F} R^{(\phi,\phi)}_{(M,N)}(\mathbf{x}_F,\mathbf{x},\omega)G^{+(\phi,\phi)}_{(N,K)}(\mathbf{x},\mathbf{x}_0,\omega)\,\mathrm{d}\mathbf{x} \tag{23}$$

where $R^{(\phi,\phi)}_{(M,N)}$ is the measured up-going M-wave potential that would have been recorded at $\mathbf{x}_F$ if there were a down-going N-component virtual source at $\mathbf{x}$, defined in a reference medium which is reflection-free above $\mathbf{x}_F$. In this equation Einstein's convention of summing repeated indices is used.

Since the goal of imaging is to estimate the zero-offset, zero-time sample of reflection responses at each subsurface point i.e., $R^{(\phi,\phi)}_{(M,N)}(\mathbf{x},\mathbf{x},t=0)$, the equation must be solved for each frequency, image point and source location. Then, all frequency components are summed to give the zero-time sample. In order to obtain this quantity, the full $R^{(\phi,\phi)}_{(M,N)}$ gather must be obtained first. This problem is usually ill posed, as one needs to estimate more quantities (the square of the number of image points) than there are equations available (the number of image points times the number of sources), and thus must be regularized. One way to do so is to consider a joint inversion with other source positions $\mathbf{x}_0$ in a procedure known as multidimensional deconvolution (MDD) (Wapenaar et al., 2008). This approach has been suggested in the presence of measured borehole recordings to eliminate the effect of the overburden (Wapenaar et al., 2008; Minato et al., 2011). Marchenko redatuming provides estimates of these recordings without the need for measurement at depth, and has been pioneered by Wapenaar et al. (2014) and Broggini et al. (2014a). The same is valid for elastic MDD (van der Neut et al., 2011), but this approach has so far not been used in connection to autofocusing. A more conventional approach is to use crosscorrelation of wavefields at each image point instead of performing an explicit inversion, and is the type of imaging that will be used hereafter.

Equation 23 remains valid if the K-potential is substituted by force or deformation sources. We therefore substitute it with a unidirectional force source in the i-direction, and evaluate the resulting equations for $M = P, S$ to write the following system of equations:

$$\begin{bmatrix} G^{-(\phi,f)}_{(P,i)} \\ G^{-(\phi,f)}_{(S,i)} \end{bmatrix} (\mathbf{x}_F, \mathbf{x}_0, \omega) = \int\limits_{\partial \mathbb{D}_F} \begin{bmatrix} R^{(\phi,\phi)}_{(P,P)} & R^{(\phi,\phi)}_{(P,S)} \\ R^{(\phi,\phi)}_{(S,P)} & R^{(\phi,\phi)}_{(S,S)} \end{bmatrix} (\mathbf{x}_F, \mathbf{x}, \omega) \begin{bmatrix} G^{+(\phi,f)}_{(P,i)} \\ G^{+(\phi,f)}_{(S,i)} \end{bmatrix} (\mathbf{x}, \mathbf{x}_0, \omega)\, \mathrm{d}\mathbf{x} \tag{24}$$

The crosscorrelational approach consists of left multiplying equation 24 by the Hermitian of the down-going field and summing over all available sources $\mathbf{x}_0$, yielding

$$\underline{\mathbf{C}}^{(f)}_{(i)}(\mathbf{x}_F, \mathbf{x}'_F, \omega) = \int\limits_{\partial \mathbb{D}_F} \underline{\mathbf{R}}(\mathbf{x}_F, \mathbf{x}, \omega) \underline{\mathbf{\Gamma}}^{(f)}_{(i)}(\mathbf{x}, \mathbf{x}'_F, \omega)\, \mathrm{d}\mathbf{x} \tag{25}$$

where the correlation function matrix is given by

$$\underline{\mathbf{C}}^{(f)}_{(i)}(\mathbf{x}_F, \mathbf{x}'_F) = \sum_{\mathbf{x}_0} \begin{bmatrix} G^{-(\phi,f)}_{(P,i)}(\mathbf{x}_F, \mathbf{x}_0) G^{+(\phi,f)*}_{(P,i)}(\mathbf{x}'_F, \mathbf{x}_0) & G^{-(\phi,f)}_{(P,i)}(\mathbf{x}_F, \mathbf{x}_0) G^{+(\phi,f)*}_{(S,i)}(\mathbf{x}'_F, \mathbf{x}_0) \\ G^{-(\phi,f)}_{(S,i)}(\mathbf{x}_F, \mathbf{x}_0) G^{+(\phi,f)*}_{(P,i)}(\mathbf{x}'_F, \mathbf{x}_0) & G^{-(\phi,f)}_{(S,i)}(\mathbf{x}_F, \mathbf{x}_0) G^{+(\phi,f)*}_{(S,i)}(\mathbf{x}'_F, \mathbf{x}_0) \end{bmatrix} \tag{26}$$

the point-spread function (PSF) matrix is given by

$$\underline{\mathbf{\Gamma}}^{(f)}_{(i)}(\mathbf{x}, \mathbf{x}'_F) = \sum_{\mathbf{x}_0} \begin{bmatrix} G^{+(\phi,f)}_{(P,i)}(\mathbf{x}, \mathbf{x}_0) G^{+(\phi,f)*}_{(P,i)}(\mathbf{x}'_F, \mathbf{x}_0) & G^{+(\phi,f)}_{(P,i)}(\mathbf{x}, \mathbf{x}_0) G^{+(\phi,f)*}_{(S,i)}(\mathbf{x}'_F, \mathbf{x}_0) \\ G^{+(\phi,f)}_{(S,i)}(\mathbf{x}, \mathbf{x}_0) G^{+(\phi,f)*}_{(P,i)}(\mathbf{x}'_F, \mathbf{x}_0) & G^{+(\phi,f)}_{(S,i)}(\mathbf{x}, \mathbf{x}_0) G^{+(\phi,f)*}_{(S,i)}(\mathbf{x}'_F, \mathbf{x}_0) \end{bmatrix} \tag{27}$$

and

$$\underline{\mathbf{R}}(\mathbf{x}_F, \mathbf{x}) = \begin{bmatrix} R^{(\phi,\phi)}_{(P,P)}(\mathbf{x}_F, \mathbf{x}) & R^{(\phi,\phi)}_{(P,S)}(\mathbf{x}_F, \mathbf{x}) \\ R^{(\phi,\phi)}_{(S,P)}(\mathbf{x}_F, \mathbf{x}) & R^{(\phi,\phi)}_{(S,S)}(\mathbf{x}_F, \mathbf{x}) \end{bmatrix} \tag{28}$$

The frequency dependencies in the above equations have been suppressed to compact the notation. With elastic MDD we to invert the PSF, while with crosscorrelational imaging we simply use the crosscorrelation function as a proxy for the reflection response, i.e. we calculate $\underline{\mathbf{C}}^{(f)}_{(i)}(\mathbf{x}_F, \mathbf{x}_F, t = 0)$ as our image at each point $\mathbf{x}_F$. Here, we will focus on the

diagonals of this correlation matrix, that is PP and SS images, by defining the following imaging conditions

$$I^{MM,ii}(\mathbf{x}_F) = \sum_{\mathbf{x}_0} \int_{-\infty}^{\infty} G^{-(\phi,f)}_{(M,i)}(\mathbf{x}_F, \mathbf{x}_0, t) G^{+(\phi,f)}_{(M,i)}(\mathbf{x}_F, \mathbf{x}_0, t)\, \mathrm{d}t \tag{29}$$

Reference Elastic Imaging

While the first arrival of the down-going wave can be modeled reasonably accurately using spatially smooth, approximate estimates of the medium parameters, modeling the up-going wavefield and the coda of the down-going wavefield using conventional methods would require the true medium parameters, including the non-smooth scattering heterogeneities. Many of these parameters are not known a priori, so most migration methods have used the surface recordings to estimate the up-going waves in the subsurface by synthetically propagating the recorded waves from the surface, backwards in time into the subsurface, a step known as wavefield extrapolation. Kirchhoff methods, for example, use ray-tracing to perform the extrapolation (Schneider, 1978; Kuo and Dai, 1984; Bleistein, 1987), while elastic reverse-time migration (RTM) (Baysal et al., 1983; Cunha, 1992; Chang and McMechan, 1994; Yan and Sava, 2008; Ravasi and Curtis, 2013) uses a wave equation to extrapolate the data backwards in time. Common to all of these methods is the use of a wavefield from a single source as the down-going wavefield, and the use of a back-propagated wavefield as the up-going wavefield. What differentiates them is how these fields are propagated or computed.

We define vectorial and tensorial reference images $I^{MM,ii}_{\mathrm{RI},v}$ and $I^{MM,ii}_{\mathrm{RI},\tau}$ respectively, based on the conventional approach of using the directly modeled direct wavefield as the down-going field in equation 30, and the back-propagated reflection data as the up-going field.

This means that in both imaging methods, we approximate the down-going field in equation 29 with

$$G^{+(\phi,f)}_{(M,i)}(\mathbf{x}_F,\mathbf{x}_0,t) \approx G^{0(\phi,f)}_{(M,i)}(\mathbf{x}_F,\mathbf{x}_0,t), \tag{30}$$

In the vectorial imaging condition, the up-going field is approximated as a simple back-propagation of a single component of the reflection data

$$G^{-(\phi,f)}_{(M,i)}(\mathbf{x}_F,\mathbf{x}_0,t) \approx \int_{\partial\mathbb{D}_0}\int_{-\infty}^{\infty} G^{-(v,f)}_{(i,i)}(\mathbf{x}_0,\mathbf{x}_0',t-\tau)G^{0(\phi,f)}_{(M,i)}(\mathbf{x}_F,\mathbf{x}_0',-\tau)\,\mathrm{d}\tau\,\mathrm{d}\mathbf{x}_0' \tag{31}$$

In the tensorial approach we inject all appropriate components from force and deformation sources at the back-propagation step:

$$G^{-(\phi,f)}_{(M,i)}(\mathbf{x}_F,\mathbf{x}_0,t) \approx \int_{\partial\mathbb{D}_0}\int_{-\infty}^{\infty} \left[\underline{\mathbf{G}}^{-}(\mathbf{x}_0',\mathbf{x}_0,t-\tau)\underline{\mathbf{G}}^{0(\phi)}_{(M)}(\mathbf{x}_F,\mathbf{x}_0,-\tau)\right]_i \mathrm{d}\tau\,\mathrm{d}\mathbf{x}_0 \tag{32}$$

where the i in notation $[\,\cdot\,]_i$ corresponds to the injected component: the first two components correspond to vertical and horizontal force sources respectively, the final two components correspond to to vertical-vertical and vertical-horizontal deformation sources, respectively.

It is relevant to note that the vectorial approach has similar theoretical propagation operators to elastic Kirchhoff methods (Kuo and Dai, 1984) and conventional elastic RTM (Chang and McMechan, 1994), where only displacement (or velocity) measurements are used to perform the wavefield extrapolation. The tensorial approach is equivalent to dynamically correct elastic RTM (Ravasi and Curtis, 2013), where the extrapolation is performed using velocity and stress recordings and force and deformation sources.

Elastic Autofocus Imaging

Historically, obtaining all required down- and up-going events including multiples at each point in the subsurface as required by equation 29, has been extremely difficult as the

multiple wavefields cannot be modeled a priori since the reflectors which generate them are not known. We have shown above how a class of commonly used methods solve this issue by ignoring down-going multiples and using a simple back-propagation of the data as the up-going field. We use this as our reference imaging method. However, as we have seen in the previous sections, autofocusing provides a data-driven way to estimate the correct up- and down-going wavefields which we may simply use with the imaging condition of equation 29. When autofocusing has been performed with the single-component approximation we refer to the imaging condition as $I^{MM,ii}_{\mathrm{AI},v}$, and when it has been produced using the original tensorial formulation we denote it as $I^{MM,ii}_{\mathrm{AI},\tau}$, where subscripts AI denote autofocus imaging. In 1D acoustic media, the acoustic version of this imaging condition has been explored by Behura et al. (2014) and Slob et al. (2014), and in 2D acoustic media by Wapenaar et al. (2014), Behura et al. (2014) and Broggini et al. (2014a,b).

It is relevant to note that autofocusing can be seen as providing an improvement to the extrapolations in equations 30, 31 and 32 which define the fields used in our reference imaging method. The source-side extrapolation step of the reference imaging method is exactly p_0^+ (or q_0^+). In vectorial reference imaging, the receiver-side back-propagation step of equation 31 is simply p_0^- (or q_0^-), as obtained in the first iteration of autofocusing for the single-component approximation. If one considers the quantities of tensorial autofocusing instead, $\underline{\mathbf{P}}_0^-$ (or $\underline{\mathbf{Q}}_0^-$) corresponds to the receiver-side tensorial extrapolation step of equation 32 in the reference tensorial imaging method. Subsequent iterations of autofocusing improve on these initial extrapolations by constructing the up- and down-going components of the entire (direct plus scattered) Green's function at $\mathbf{x}_F$. As such, autofocus imaging provides a way to utilize correctly the multiply scattered energy in the data, by creating the appropriate extrapolated wavefields at each point in the subsurface.

Nevertheless, crosstalk between unrelated up- and down-going events may causes artifacts in autofocus imaging, even if these fields have been estimated correctly. Since there are more events in propagated wavefields with multiples than in wavefields that only include direct waves, this effect may be significant. In particular, this may create spurious reflectors in the image, as will be shown below. In order to minimize these effects, deconvolution-based imaging conditions such as elastic MDD may be used to attenuate them, but are computationally more expensive.

Another way to mitigate these effects is to use an intermediate method that has elements of both conventional and autofocus imaging, by taking the zero-time crosscorrelation between the autofocused up-going field $G^{-(\phi,f)}_{(M,i)}(\mathbf{x}_F, \mathbf{x}_0, t)$, and only the direct down-going wave $G^{0(\phi,f)}_{(M,i)}(\mathbf{x}, \mathbf{x}_0, t)$ based on the work of Wapenaar et al. (1987). We will denote these imaging conditions by $I^{MM,ii}_{\mathrm{dAI},v}$ and $I^{MM,ii}_{\mathrm{dAI},\tau}$, where subscripts dAI denotes direct-wave autofocus imaging, and the v and τ subscripts refer to how the up-going field was estimated, either by single-component or tensorial autofocusing, respectively. While in effect we discard some of the information provided by autofocusing (the scattered down-going field), we show below that this imaging condition out-performs autofocus and reference imaging in our numerical example by removing crosstalk between up- and down-going multiples while still using the (up-going) multiple energy for imaging.

NUMERICAL RESULTS

In order to compare reference and autofocus imaging methods we use a 2D solid-Earth elastic model with lateral and vertical density variations shown in Figure 2. P- and S-wave velocities are constant at 2.7 km/s and 1.5 km/s, respectively. Constant velocities simply provide an easier setting in which to interpret arrivals, and are not necessary to the

application of the method.

[Figure 2 about here.]

All imaging methods discussed above require as input the direct wave from the source at each subsurface point. Since the velocities were constant in the model we use in this study, the source wavefields were constructed analytically by calculating the traveltimes and inserting a Ricker wavelet of constant amplitude with a central frequency of 20 Hz at appropriate arrival times, with a phase reversal on traces to the right of the trace of smallest traveltime for x components of the P-wave and z components of the S-wave. Improved results may be obtained by carefully introducing geometrical spreading and the $\pi/4$ phase shift characteristic of the 2D Green's functions (Thorbecke et al., 2013). This method is not generalizable to variable velocity media but a variety of other methods can then be used: ray-tracing (dynamic or otherwise) (Červený, 2001), eikonal solvers (Vidale, 1988) and Huygens wavefront tracing (Sava and Fomel, 2001) provide fast computation of direct arrivals or their traveltimes in heterogenous media. Furthermore, for arbitrarily complex media where those methods might not be appropriate, highly accurate arrivals can be computed using finite difference methods (Virieux, 1984, 1986).

The imaging methods also require the up-going scattered wavefield at the surface. Data recorded with a wideband, wide aperture and densely sampled seismic acquisition with collocated sources and receivers that has undergone removal of the direct wave, source or receiver ghosts, surface-related multiples and ground-roll can be used as a proxy. For this numerical example, this was achieved by finite difference modeling (Virieux, 1984) in the true and smoothed media, followed by subtraction of the two responses; this procedure removes the direct wave leaving only the up-going scattered field. To remove surface-waves,

an f-k filter was applied. In addition, absorbing boundary conditions guarantee that no surface-related multiples or ghosts are present. The above theory assumes delta function sources, and thus we deconvolve the source wavelet from the reflection data prior to imaging.

[Figure 3 about here.]

da Costa et al. (2014a) showed examples of the P and S wavefields extrapolated to subsurface image points using autofocusing, and Figure 3 shows more examples of P- and S-wave Green's functions from image point $\mathbf{x}_F$ in Figure 2 obtained both from direct modeling and from the two elastic autofocusing schemes presented above — single-component and fully tensorial. It is relevant to note that while we show $\mathbf{x}_F$ as a virtual receiver in the equations above, we show Green's functions in Figure 3 as if it were the location of a subsurface source; the equivalence between these two representations is proved by the elastic source-receiver reciprocity theorem (Wapenaar and Fokkema, 2006)

$$G^{(v,\phi)}_{(i,M)}(\mathbf{x}_0, \mathbf{x}_F, t) = G^{(\phi,f)}_{(M,i)}(\mathbf{x}_F, \mathbf{x}_0, t) \tag{33}$$

While there are errors in the extrapolated fields, especially in those using the single-component approximation, it is clear that autofocusing performs well at estimating subsurface scattered fields, and that fully tensorial autofocusing outperforms single-component autofocusing of both P- and S-waves.

The PP reference image in Figure 4 was generated using imaging condition $I^{PP,zz}_{\mathrm{RI},v}$, the PP autofocus image in Figure 5 using imaging condition $I^{PP,zz}_{\mathrm{AI},v}$, and the direct-wave autofocus PP image in Figure 6 using the imaging condition $I^{PP,zz}_{\mathrm{dAI},v}$.

[Figure 4 about here.]

[Figure 5 about here.]

[Figure 6 about here.]

[Figure 7 about here.]

[Figure 8 about here.]

[Figure 9 about here.]

[Figure 10 about here.]

[Figure 11 about here.]

The SS images were obtained similarly, however, the corresponding imaging conditions were $I^{SS,xx}_{\mathrm{RI},v}$ (Figure 7), $I^{SS,xx}_{\mathrm{AI},v}$ (Figure 8) and $I^{SS,xx}_{\mathrm{dAI},v}$ (Figure 9), all of which used instead the horizontal component of the recorded velocity data as it provides better quality recordings of S-waves. No smoothing or filtering has been applied to any of the images.

We also image the portion of the model inside the white dotted box in Figure 2 using the tensorial imaging conditions $I^{PP,zz}_{\mathrm{RI},\tau}$, $I^{PP,zz}_{\mathrm{AI},\tau}$ and $I^{PP,zz}_{\mathrm{dAI}\tau}$ which are all shown in Figure 10, and $I^{SS,xx}_{\mathrm{RI},\tau}$, $I^{SS,xx}_{\mathrm{AI},\tau}$ and $I^{SS,xx}_{\mathrm{dAI},\tau}$ are shown in Figure 11. These images are of fundamental importance to aid our understanding of the limitations of the single-component approximation. Since they require stress recordings they are currently only practically applicable where stress can be related to strain and where that strain can be measured, for example when using ocean-bottom cables (e.g., Ravasi and Curtis, 2013). However, they also show the potential improvements that could be realized if such stress or strain measurements were to become more generally available.

DISCUSSION

The reference, autofocus and direct-wave autofocus images all show a recovery of the true subsurface interfaces as shown by the solid curves in Figures 4 through 9. In the reference images, spurious reflectors are generated by the correlation between the source wavefield (direct wave) and the back-propagated multiple reflections (Guitton et al., 2007). Both reference PP and SS images exhibit spurious reflectors, as shown by the dashed curves in Figures 4 and 7: for example, the synclinal reflector is seen to repeat at least four times on the latter figure. Figure 12a contains a schematic diagram depicting why this occurs for the first ghost reflector (counting from top to bottom): the solid lines represent the raypath of an internal multiple contained in the reflection, which is mistaken for a primary (dashed black line) reflecting off of a ghost reflector (dotted white line).

Another such event is shown under the second dashed curve in Figures 4 and 7. The types of raypaths that interact to create that artifact are shown by the thicker solid black ray in Figure 12b. The white ray represents the direct wave whose zero-offset traveltime is 0.32 s. The thick solid black ray represents a single event in the back-propagated reflection data which, because of the geometry of the model, also has a zero-offset traveltime of 0.32 s. Figure 12b also explains how this event is generated: the solid black (thin and thick) ray represents the raypath present in the scattered up-going field at the surface $G^{-(v,f)}_{(z,z)}(\mathbf{x}'_0, \mathbf{x}_0, t)$, while the dashed black ray represents the time-reversed direct wave. The back-propagation step will cause the traveltime of the direct wave to be removed from that of the reflections, canceling the solid and dashed thin black lines in Figure 12b. The resulting event is generated by waves traveling along the thick black ray, but has the same traveltime as that of a direct wave recorded at the white imaging point, and thus creates

spurious energy in the image at that point.

[Figure 12 about here.]

Autofocus imaging, on the other hand, eliminates most of these artifacts by placing internal multiples correctly in their respective up- and down-going fields. As a consequence, around the center of the imaging region the spurious reflectors such as those previously indicated by the dashed curves in Figures 4 and 7 are greatly attenuated in Figures 5 and 8. However, Figures 5 and 8 are not entirely devoid of spurious reflectors — the dashed curves show other spurious reflectors in these images. This is because the crosstalk interactions between events with different wavepaths but equal traveltimes may also cause artifacts in autofocus imaging. The raypaths that correlate to cause the first spurious reflector (counting from top to bottom) are shown in Figure 12c. The white raypath shows a down-going internal multiple present and the black raypath represents an up-going primary present. Both events arrive exactly at 0.23 s and interfere constructively to create the spurious reflector, even though the events are unrelated.

These sorts of interactions are model dependent and unavoidable when using correlation-type imaging conditions, but may be attenuated by using deconvolution imaging conditions (Wapenaar et al., 2008, 2014; Broggini et al., 2014a). However, while still using correlation imaging condition, direct-wave autofocus imaging avoids these kinematic artifacts by using only the direct-wave as a down-going field, but using the estimated scattered up-going field obtained from elastic autofocusing. This is seen in Figures 6 and 9, in which the aforementioned artifacts around the center of the model are severely attenuated.

Nevertheless, other artifacts are still present, especially away from the center of the model. In order to understand these artifacts, we draw attention to the section of the

model enclosed by the white dotted box in Figure 2 as shown in the images of Figure 10 and 11. We observe artifacts from the synclinal interface in the three PP imaging schemes which use the single-component approximation (Figures 10a, b and c) as well as in the SS images (Figures 11a, b and c). The fact that they appear in the autofocus and direct-wave autofocus imaging schemes, as well as in the reference images, precludes them from being solely attributed to the Born (single-scattering) approximation. Indeed, in the single-component approximation in Appendix C, it was assumed that the waves travel mostly in the vertical direction, which fails for internal multiples that interact with the synclinal interface away from the center. Therefore, most of the dipping artifacts in Figure 10b, c and Figure 11b, c result from the single-component approximation. This approximation also affects the reference images (Figures 10a and 11a), which is further harmed by the Born approximation. This explains why, when considering the tensorial PP images (Figure 10d, e) and tensorial SS images (Figures 11d, e), these dipping artifacts are attenuated. This is true for both autofocus and direct-wave autofocus imaging, where we notice that almost all dipping artifacts disappear from the PP images (Figure 10e, f). Furthermore, direct-wave autofocus imaging also outperforms autofocus imaging in the tensorial formulations, where we observe fewer artifacts when comparing Figure 10e to 10f and Figure 11e to 11f.

While presently stress measurements and deformation sources in field data are not readily available, it was noted above that by considering homogenous and isotropic media at the surface acquisition datum, we may instead only require velocity and force sources, provided that estimates of elastic medium parameters (λ and μ) are known, reducing the need of 36 Green's functions components to 9 components in 3D media. This has not yet been attempted on real data. A similar approach using P and S wave potentials (Wapenaar and Slob, 2014; Wapenaar, 2014) shows it may be feasible, though this approach requires the

decomposition of the data into P and S wave source and receiver potentials.

Despite the improvements introduced by the use of tensorial autofocusing and the direct-wave autofocus imaging conditions, a few artifacts can still be seen between the upper two true reflectors in Figure 10f and Figure 11f. Some of these artifacts are essentially the same as shown in Figure 12b which have not been properly attenuated and thus have contaminated the up-going field. Imperfect reconstruction of the Green's functions may also be caused by other factors, including the lack of conversions in the initial estimate of the Green's functions as discussed above, and by the incorrect separation of physical and nonphysical events introduced by the time-windowing before the direct wave. Furthermore, in SS images, the imaging condition introduces other artifacts since physical SP conversions from image points that do not lie on reflectors may have the same traveltime as the direct-wave, causing spurious structure to be imaged.

Nevertheless, as can be seen in the comparisons above, autofocus and direct-wave autofocus imaging improve greatly over the reference images based on conventional methods by diminishing the amount of internal-multiple related artifacts that may hamper interpretation of seismic images. The use of horizontal components of the Green's function leads to even better images, as demonstrated by the tensorial imaging conditions above.

CONCLUSION

We present data-driven nonlinear imaging methods for isotropic elastic solid media based on the complete theory of elastic autofocusing, and a single-component approximation that is more suitable for real seismic acquisition. We contrast the results with reference imaging methods based on conventional migration by imaging a subsurface model with lateral

and vertical density variations and constant P- and S-wave velocities. We observe that the P- and S-wave autofocus imaging method considerably attenuates artifacts that are often present in conventional imaging approaches, caused by internal multiply-scattered energy. Furthermore, the proposed direct-wave autofocus imaging method attenuates artifacts caused by the crosstalk between unrelated events that are still present in previous autofocus imaging methods.

ACKNOWLEDGMENTS

The authors thank the Edinburgh Interferometry Project sponsors (ConocoPhillips, Schlumberger Gould Research, Statoil and Total) for supporting this research. The first author would also like to thank CAPES for research funding. The authors also extend their thanks to the Editor, to Kees Wapenaar of Delft University of Technology for several fruitful discussions and suggestions, and to Fillipo Broggini and an anonymous reviewer for their insightful comments.

APPENDIX A

RELATION BETWEEN FOCUSING AND TRANSMISSION FUNCTIONS

The representation of elastodynamic Green's functions in terms of focusing functions (da Costa et al., 2014a) is stated as follows:

$$G^{-(v,f)}_{(p,q)}(\mathbf{x}_F,\mathbf{x}'_0,\omega) = -F^{-(v,f)}_{(q,p)}(\mathbf{x}'_0,\mathbf{x}_F,\omega) + \int\limits_{\partial\mathbb{D}_0} \big\{G^{-(v,h)}_{(q,iz)}(\mathbf{x}'_0,\mathbf{x}_0,\omega)F^{+(v,f)}_{(i,p)}(\mathbf{x}_0,\mathbf{x}_F,\omega) - G^{-(v,f)}_{(q,i)}(\mathbf{x}'_0,\mathbf{x}_0,\omega)F^{+(\tau,f)}_{(iz,p)}(\mathbf{x}_0,\mathbf{x}_F,\omega)\big\}\,\mathrm{d}^2\mathbf{x}_0 \quad \text{(A-1)}$$

$$G^{+(v,f)}_{(p,q)}(\mathbf{x}_F,\mathbf{x}'_0,\omega) = F^{+(v,f)*}_{(q,p)}(\mathbf{x}'_0,\mathbf{x}_F,\omega) - \int\limits_{\partial\mathbb{D}_0} \big\{G^{-(v,h)}_{(q,iz)}(\mathbf{x}'_0,\mathbf{x}_0,\omega)F^{-(v,f)*}_{(i,p)}(\mathbf{x}_0,\mathbf{x}_F,\omega) + G^{-(v,f)}_{(q,i)}(\mathbf{x}'_0,\mathbf{x}_0,\omega)F^{-(\tau,f)*}_{(iz,p)}(\mathbf{x}_0,\mathbf{x}_F,\omega)\big\}\,\mathrm{d}^2\mathbf{x}_0 \quad \text{(A-2)}$$

where G is the elastodynamic Green's function as defined in the main text, and F is an acausal solution of the sourceless elastodynamic wave equation which focuses at $\mathbf{x}_F$ at zero-time. This function is defined in a reference medium that is reflection-free under the datum containing $\mathbf{x}_F$ and the condition of its focusing is expressed by the following equation (da Costa et al., 2014a):

$$F^{+(\tau,f)}_{(iz,p)}(\mathbf{x}'_F,\mathbf{x}_F,\omega) = -\frac{1}{2}\delta_{ip}\delta(\mathbf{x}'_F - \mathbf{x}_F)\big|_{z=0} \quad \text{(A-3)}$$

Equations A-1 and A-2 relate the down- and up-going fields of the Green's function at $\mathbf{x}_F$ from force sources at $\mathbf{x}'_0$ to the focusing functions F and the up-going (scattered) field at $\mathbf{x}'_0$. We may sum the equations, and simplify the sum by defining the following auxiliary focusing function

$$H^{(v,f)}_{(p,j)}(\mathbf{x}_F,\mathbf{x},\omega) = F^{+(v,f)}_{(j,p)}(\mathbf{x},\mathbf{x}_F,\omega) - F^{-(v,f)*}_{(j,p)}(\mathbf{x},\mathbf{x}_F,\omega) \quad \text{(A-4)}$$

After obtaining the stresses from the generalized Hooke's law (equation 3), we condense the obtained simplification into the vector valued equality of equation 4 which we have referred to as the representation theorem. Therefore, H is a combination of the up- and down-going components of F, itself a focusing function. In order to relate the transmission operator to H, we will first relate it to F.

We start with the two-way elastodynamic representation theorem (Wapenaar and Fokkema, 2006) for two wavestates A and B defined within $\partial\mathbb{D}$

$$\oint\limits_{\partial\mathbb{D}} \{v^B_i\tau^A_{ij} - \tau^B_{ij}v^A_i\}n_j\,\mathrm{d}^2\mathbf{x} = 0 \quad \text{(A-5)}$$

and assume that $\partial\mathbb{D}$ is composed by two infinite horizontal planes $\partial\mathbb{D}_0$ and $\partial\mathbb{D}_F$, where $\partial\mathbb{D}_0$ is the acquisition surface datum containing $\mathbf{x}_0$ and $\partial\mathbb{D}_F$ is the datum containing $\mathbf{x}_F$ to obtain

$$\int_{\partial\mathbb{D}_0} \{v_i^B \tau_{iz}^A - \tau_{iz}^B v_i^A\}\, \mathrm{d}^2\mathbf{x}_0 = \int_{\partial\mathbb{D}_F} \{v_i^B \tau_{iz}^A - \tau_{iz}^B v_i^A\}\, \mathrm{d}^2\mathbf{x}'_F \tag{A-6}$$

We further simplify this expression by considering one-way wavefields that under certain conditions (Wapenaar and Haimé, 1990) lead to

$$-2\int_{\partial\mathbb{D}_0} \{v_i^{B+} \tau_{iz}^{A-} - \tau_{iz}^{B-} v_i^{A+}\}\, \mathrm{d}^2\mathbf{x}_0 = 2\int_{\partial\mathbb{D}_F} \{v_i^{B-} \tau_{iz}^{A+} - \tau_{iz}^{B+} v_i^{A-}\}\, \mathrm{d}^2\mathbf{x}'_F \tag{A-7}$$

We take wavestate A to represent the transmission T from a unidirectional force source in the q-direction from $\mathbf{x}''_F$ to the surface, and wavestate B to represents the function F with focusing condition defined by equation A-3. Equation A-7 can be written as

$$\begin{aligned} &-2\int_{\partial\mathbb{D}_0} \{F_{(i,p)}^{+(v,f)}(\mathbf{x}_0,\mathbf{x}_F) T_{(iz,q)}^{-(\tau,f)}(\mathbf{x}_0,\mathbf{x}''_F) - F_{(iz,p)}^{-(\tau,f)}(\mathbf{x}_0,\mathbf{x}_F) T_{(i,q)}^{+(v,f)}(\mathbf{x}_0,\mathbf{x}''_F)\}\, \mathrm{d}^2\mathbf{x}_0 \\ &= 2\int_{\partial\mathbb{D}_F} \{F_{(i,p)}^{-(v,f)}(\mathbf{x}'_F,\mathbf{x}_F) T_{(iz,q)}^{+(\tau,f)}(\mathbf{x}'_F,\mathbf{x}''_F) - F_{(iz,p)}^{+(\tau,f)}(\mathbf{x}'_F,\mathbf{x}_F) T_{(i,q)}^{-(v,f)}(\mathbf{x}'_F,\mathbf{x}''_F)\}\, \mathrm{d}^2\mathbf{x}'_F \end{aligned} \tag{A-8}$$

Since the medium is homogenous above $\partial\mathbb{D}_0$, we have that on the LHS of equation A-8, $T_{(i,q)}^{+(v,f)}(\mathbf{x}_0,\mathbf{x}''_F) = 0$ and $T_{(iz,q)}^{-(\tau,f)}(\mathbf{x}_0,\mathbf{x}''_F) = T_{(iz,q)}^{(\tau,f)}(\mathbf{x}_0,\mathbf{x}''_F)$, that is, there is no down-going transmission response at $\partial\mathbb{D}_0$. Since F is defined in a reference medium which is reflection-free below $\partial\mathbb{D}_F$, on the right-hand side of equation A-7, $F_{(i,p)}^{-(v,f)}(\mathbf{x}'_F,\mathbf{x}_F) = 0$. Furthermore, from the definition of the transmission response, $T_{(i,q)}^{-(v,f)}(\mathbf{x}'_F,\mathbf{x}''_F) = \delta(\mathbf{x}'_F - \mathbf{x}''_F)\delta_{iq}$. We apply these considerations and the focusing condition for F (equation A-3) to equation A-8:

$$-2\int_{\partial\mathbb{D}_0} F_{(i,p)}^{+(v,f)}(\mathbf{x}_0,\mathbf{x}_F) T_{(iz,q)}^{(\tau,f)}(\mathbf{x}_0,\mathbf{x}''_F)\, \mathrm{d}^2\mathbf{x}_0 = 2\int_{\partial\mathbb{D}_F} -\left(-\frac{1}{2}\delta_{ip}\delta(\mathbf{x}'_F - \mathbf{x}_F)\right)\delta(\mathbf{x}'_F - \mathbf{x}''_F)\delta_{iq}\, \mathrm{d}^2\mathbf{x}'_F \tag{A-9}$$

or simply

$$\int_{\partial\mathbb{D}_0} F_{(i,p)}^{+(v,f)}(\mathbf{x}_0,\mathbf{x}_F) T_{(iz,q)}^{(\tau,f)}(\mathbf{x}_0,\mathbf{x}''_F)\, \mathrm{d}^2\mathbf{x}_0 = -\frac{1}{2}\delta_{pq}\delta(\mathbf{x}''_F - \mathbf{x}_F) \tag{A-10}$$

This equation states in which sense F^+ is the inverse of the transmission operator. According to equation A-4, H is a sum of F^+ and F^-, and thus, an initial estimate of H should reflect that F^+ is the inverse of the transmission, containing converted events.

APPENDIX B

Q AUTOFOCUSING

In layered acoustic media, it has been shown that a modified autofocusing algorithms yields the difference between up- and down-going Green's functions, as opposed to their sum (Broggini et al., 2014b). Here we establish this algorithm in the elastic case, starting from the decomposed Marchenko equations (Slob et al., 2014) that are provided for elastodynamic Green's functions in equations A-1 and A-2 If we subtract one from the other, we obtain

$$G^{+(v,f)}_{(p,q)}(\mathbf{x}_F,\mathbf{x}'_0,\omega) - G^{-(v,f)}_{(p,q)}(\mathbf{x}_F,\mathbf{x}'_0,\omega) = \bar{H}^{(v,f)*}_{(p,q)}(\mathbf{x}_F,\mathbf{x}'_0,\omega) -$$
$$\int\limits_{\partial\mathbb{D}_0} \left\{ G^{-(v,h)}_{(q,iz)}(\mathbf{x}'_0,\mathbf{x}_0,\omega)\bar{H}^{(v,f)}_{(p,i)}(\mathbf{x}_F,\mathbf{x}_0,\omega) - G^{-(v,f)}_{(q,i)}(\mathbf{x}'_0,\mathbf{x}_0,\omega)\bar{H}^{(v,h)}_{(p,iz)}(\mathbf{x}_F,\mathbf{x}_0,\omega) \right\} \mathrm{d}^2\mathbf{x}_0 \quad \text{(B-1)}$$

where

$$\bar{H}^{(v,f)}_{(p,j)}(\mathbf{x}_F,\mathbf{x},\omega) = F^{+(v,f)}_{(j,p)}(\mathbf{x},\mathbf{x}_F,\omega) + F^{-(v,f)*}_{(j,p)}(\mathbf{x},\mathbf{x}_F,\omega) \quad \text{(B-2)}$$

From equation B-1 it is not difficult to show that after taking the receiver-side N potential, the difference between the down- and up-going functions satisfies the following representation theorem in the time domain:

$$\underline{\mathbf{G}}^{+(\phi)}_{(N)}(\mathbf{x}_F,\mathbf{x}'_0,t) - \underline{\mathbf{G}}^{-(\phi)}_{(N)}(\mathbf{x}_F,\mathbf{x}'_0,t) = \underline{\bar{\mathbf{H}}}^{(\phi)}_{(N)}(\mathbf{x}_F,\mathbf{x}'_0,-t) -$$
$$\int\limits_{\partial\mathbb{D}_0}\int\limits_{-\infty}^{\infty} \underline{\mathbf{G}}^{-}(\mathbf{x}'_0,\mathbf{x}_0,t-\tau)\,\underline{\bar{\mathbf{H}}}^{(\phi)}_{(N)}(\mathbf{x}_F,\mathbf{x}_0,\tau)\,\mathrm{d}\tau\,\mathrm{d}^2\mathbf{x}_0 \quad \text{(B-3)}$$

where

$$\underline{\bar{\mathbf{H}}}^{(\phi)}_{(N)} = \left(\bar{H}^{(\phi,f)}_{(N,x)}\ \bar{H}^{(\phi,f)}_{(N,y)}\ \bar{H}^{(\phi,f)}_{(N,z)}\ -\bar{H}^{(\phi,h)}_{(N,xz)}\ -\bar{H}^{(\phi,h)}_{(N,yz)}\ -\bar{H}^{(\phi,h)}_{(N,zz)}\right)^T \quad \text{(B-4)}$$

This representation theorem is very similar to the one obtained previously. In fact, we use the same method to solve it. By proposing the following ansatz

$$\underline{\bar{\mathbf{H}}}^{(\phi)}_{(N)}(\mathbf{x}_F,\mathbf{x}_0,t)=\underline{\mathbf{G}}^{0(\phi)}_{(N)}(\mathbf{x}_F,\mathbf{x}_0,-t)-\theta(t+t^0_{(N)}(\mathbf{x}_F,\mathbf{x}_0))\,\underline{\bar{\mathbf{M}}}^{(\phi)}_{(N)}(\mathbf{x}_F,\mathbf{x}_0,t) \tag{B-5}$$

we may derive another Marchenko equation:

$$\begin{aligned}\mathbf{0}=&\int_{\partial\mathbb{D}_0}\int_{-\infty}^{\infty}\underline{\mathbf{G}}^{-}(\mathbf{x}_0',\mathbf{x}_0,t-\tau)\underline{\mathbf{G}}^{0(\phi)}_{(N)}(\mathbf{x}_F,\mathbf{x}_0,-\tau)\,\mathrm{d}\tau\,\mathrm{d}^2\mathbf{x}_0\\&-\int_{\partial\mathbb{D}_0}\int_{-t^0_{(N)}}^{\infty}\underline{\mathbf{G}}^{-}(\mathbf{x}_0',\mathbf{x}_0,t-\tau)\underline{\bar{\mathbf{M}}}^{(\phi)}_{(N)}(\mathbf{x}_F,\mathbf{x}_0,\tau)\,\mathrm{d}\tau\,\mathrm{d}^2\mathbf{x}_0+\underline{\bar{\mathbf{M}}}^{(\phi)}_{(N)}(\mathbf{x}_F,\mathbf{x}_0',-t)\end{aligned} \tag{B-6}$$

It is straightforward to show that the iteration into equations 13 and 14 solves the Marchenko equation B-6, and at convergence, $\underline{\mathbf{Q}}^{-}(\mathbf{x}_F,\mathbf{x}_0,t)=-\underline{\bar{\mathbf{M}}}^{(\phi)}_{(N)}(\mathbf{x}_F,\mathbf{x}_0',-t)$. Inserting terms $\underline{\mathbf{Q}}^{-}(\mathbf{x}_F,\mathbf{x}_0,t)$ and $\underline{\mathbf{Q}}^{+}(\mathbf{x}_F,\mathbf{x}_0,-t)$ in equations B-5 and B-3 we obtain the reconstruction of the Green's functions according to equation 15.

APPENDIX C

SINGLE-COMPONENT AUTOFOCUSING

In an arbitrarily inhomogeneous anisotropic medium the following representation theorem is given by da Costa et al. (2014a):

$$\begin{aligned}G^{(v,f)}_{(p,q)}(\mathbf{x}_F,\mathbf{x}_0',\omega)=H^{(v,f)*}_{(p,q)}(\mathbf{x}_F,\mathbf{x}_0',\omega)+\int_{\partial\mathbb{D}_0}\{&G^{-(v,h)}_{(q,iz)}(\mathbf{x}_0',\mathbf{x}_0,\omega)H^{(v,f)}_{(p,i)}(\mathbf{x}_F,\mathbf{x}_0,\omega)-\\&G^{-(v,f)}_{(q,i)}(\mathbf{x}_0',\mathbf{x}_0,\omega)H^{(v,h)}_{(p,iz)}(\mathbf{x}_F,\mathbf{x}_0,\omega)\}\,\mathrm{d}^2\mathbf{x}_0\end{aligned} \tag{C-1}$$

where according to Hooke's law in equation 3,

$$G^{-(v,h)}_{(q,ij)}(\mathbf{x}_0',\mathbf{x}_0,\omega)=(\iota\omega)^{-1}c_{ijkl}(\mathbf{x}_0)\partial_l G^{-(v,f)}_{(q,k)}(\mathbf{x}_0',\mathbf{x}_0,\omega) \tag{C-2}$$

$$H^{(v,h)}_{(p,ij)}(\mathbf{x}_F,\mathbf{x}_0,\omega)=(\iota\omega)^{-1}c_{ijkl}(\mathbf{x}_0)\partial_l H^{(v,f)}_{(p,k)}(\mathbf{x}_F,\mathbf{x}_0,\omega) \tag{C-3}$$

where the derivative ∂_l is always taken over the coordinate $\mathbf{x}_0$. We consider that around the (source) location $\mathbf{x}_0$ the medium is isotropic and shearless, that is,

$$c_{ijkl}(\mathbf{x}_0) = \lambda(\mathbf{x}_0)\delta_{ij}\delta_{kl} \tag{C-4}$$

where $\lambda(\mathbf{x}_0)$ is the first Lamé parameter and δ is the Kronecker delta, but can be arbitrarily inhomogeneous and anisotropic elsewhere. Substituting equations C-2 and C-3 into the representation theorem of equation C-1, and substituting the stiffness relation of equation C-4 for $q = z$ into the resulting expression, we obtain

$$G^{(v,f)}_{(p,z)}(\mathbf{x}_F, \mathbf{x}'_0, \omega) = H^{(v,f)*}_{(p,z)}(\mathbf{x}_F, \mathbf{x}'_0, \omega) + (\iota\omega)^{-1} \int\limits_{\partial\mathbb{D}_0} \lambda(\mathbf{x}_0) \big\{ \partial_k G^{-(v,f)}_{(z,k)}(\mathbf{x}'_0, \mathbf{x}_0, \omega) H^{(v,f)}_{(p,z)}(\mathbf{x}_F, \mathbf{x}_0, \omega) - G^{-(v,f)}_{(z,z)}(\mathbf{x}_0, \mathbf{x}'_0, \omega) \partial_k H^{(v,f)}_{(p,k)}(\mathbf{x}_F, \mathbf{x}_0, \omega) \big\} \, \mathrm{d}^2\mathbf{x}_0 \tag{C-5}$$

If now we consider that the medium is isotropic (possibly with shear) around $\mathbf{x}_F$, by applying the appropriate differential operator (Wapenaar and Haimé, 1990) we obtain the following equation using P-wave potentials at $\mathbf{x}_F$:

$$G^{(\phi,f)}_{(P,z)}(\mathbf{x}_F, \mathbf{x}'_0, \omega) = H^{(\phi,f)*}_{(P,z)}(\mathbf{x}_F, \mathbf{x}'_0, \omega) + (\iota\omega)^{-1} \int\limits_{\partial\mathbb{D}_0} \lambda(\mathbf{x}_0) \big\{ \partial_k G^{-(v,f)}_{(z,k)}(\mathbf{x}'_0, \mathbf{x}_0, \omega) H^{(\phi,v)}_{(P,z)}(\mathbf{x}_F, \mathbf{x}_0, \omega) - G^{-(v,f)}_{(z,z)}(\mathbf{x}'_0, \mathbf{x}_0, \omega) \partial_k H^{(\phi,f)}_{(P,k)}(\mathbf{x}_F, \mathbf{x}_0, \omega) \big\} \, \mathrm{d}^2\mathbf{x}_0 \tag{C-6}$$

We impose far-field approximations to G^- and H which suppose that at the surface $\partial\mathbb{D}_0$ the energy emanates mainly in the vertical direction:

$$\partial_k G^{-(v,f)}_{(z,k)}(\mathbf{x}'_0, \mathbf{x}_0, \omega) \approx -\delta_{kz} \frac{\iota\omega}{c_P(\mathbf{x}_0)} G^{-(v,f)}_{(z,k)}(\mathbf{x}'_0, \mathbf{x}_0, \omega) \tag{C-7}$$

$$\partial_k H^{(\phi,f)}_{(P,k)}(\mathbf{x}_F, \mathbf{x}_0, \omega) \approx \delta_{kz} \frac{\iota\omega}{c_P(\mathbf{x}_0)} H^{(\phi,v)}_{(P,k)}(\mathbf{x}_F, \mathbf{x}_0, \omega) \tag{C-8}$$

where $c_P(\mathbf{x}_0) = \sqrt{\lambda(\mathbf{x}_0)/\rho(\mathbf{x}_0)}$ is the P-wave velocity at the surface, δ_{kz} is the Kronecker delta, and the spatial derivatives ∂_k are taken in the $\mathbf{x}_0$ coordinate. Inserting approximations

of equations C-7 and C-8 into equation C-9 yields

$$G^{(\phi,f)}_{(P,z)}(\mathbf{x}_F, \mathbf{x}'_0, \omega) = H^{(\phi,f)*}_{(P,z)}(\mathbf{x}_F, \mathbf{x}'_0, \omega) + \int_{\partial\mathbb{D}_0} 2\frac{\rho(\mathbf{x}_0)}{c_P(\mathbf{x}_0)} G^{-(v,f)}_{(z,z)}(\mathbf{x}'_0, \mathbf{x}_0, \omega) H^{(\phi,f)}_{(P,z)}(\mathbf{x}_F, \mathbf{x}_0, \omega)\, \mathrm{d}^2\mathbf{x}_0 \quad \text{(C-9)}$$

REFERENCES

Abma, R., N. Kabir, K. H. Matson, S. Michell, S. A. Shaw, and B. McLain, 2005, Comparisons of adaptive subtraction methods for multiple attenuation: The Leading Edge, **24**, 277–280.

Amundsen, L., 2001, Elimination of freesurface related multiples without need of the source wavelet: Geophysics, **66**, 327–341.

Baysal, E., D. D. Kosloff, and J. W. C. Sherwood, 1983, Reverse time migration: Geophysics, **48**, 1514–1524.

Behura, J., K. Wapenaar, and R. Snieder, 2014, Autofocus Imaging: Image reconstruction based on inverse scattering theory: Geophysics, **79**, A19–A26.

Berkhout, A. J., 2012, Combining full wavefield migration and full waveform inversion, a glance into the future of seismic imaging: Geophysics, **77**, S43–S50.

Berkhout, A. J., and D. J. Verschuur, 2005, Removal of internal multiples with the common-focus-point (CFP) approach: Part 1 Explanation of the theory: Geophysics, **70**, V45–V60.

———, 2006, Imaging of multiple reflections: Geophysics, **71**, SI209–SI220.

Bleistein, N., 1987, On the imaging of reflectors in the earth: Geophysics, **52**, 931–942.

Broggini, F., R. Snieder, and K. Wapenaar, 2012, Focusing the wavefield inside an unknown 1D medium: Beyond seismic interferometry: Geophysics, **77**, A25–A28.

———, 2014a, Data-driven wavefield focusing and imaging with multidimensional deconvolution: Numerical examples for reflection data with internal multiples: Geophysics, **79**, WA107–WA115.

Broggini, F., K. Wapenaar, J. van der Neut, and R. Snieder, 2014b, Data-driven Green's function retrieval and application to imaging with multidimensional deconvolution: Jour-

nal of Geophysical Research: Solid Earth, **119**, 425–441.

Brown, M. P., and A. Guitton, 2005, Least-squares joint imaging of multiples and primaries: Geophysics, **70**, S79–S89.

Červený, V., 2001, Seismic Ray Theory: Cambridge University Press.

Chang, W., and G. A. McMechan, 1986, Reverse-time migration of offset vertical seismic profiling data using the excitation-time imaging condition: Geophysics, **51**, 67–84.

———, 1994, 3-D elastic prestack, reverse-time depth migration: Geophysics, **59**, 597–609.

Chapman, C. H., 2004, Fundamentals of Seismic Wave Propagation: Cambridge University Press.

Claerbout, J. F., 1971, Toward a Unified Theory of Reflector Mapping: Geophysics, **36**, 467–481.

Cunha Filho, C. A., 1992, Elastic Modeling and Migration in Earth Models: Phd, Stanford University.

da Costa Filho, C. A., M. Ravasi, A. Curtis, and G. A. Meles, 2014a, Elastodynamic Green's function retrieval through single-sided Marchenko inverse scattering: Physical Review E, **90**, 063201.

da Costa Filho, C. A., M. Ravasi, G. Meles, and A. Curtis, 2014b, Elastic Autofocusing: 76th EAGE Conference & Exhibition.

———, 2014c, Elastic autofocusing via single-sided Marchenko inverse scattering: SEG Technical Program Expanded Abstracts 2014, 4603–4607.

Fleury, C., 2013, Increasing illumination and sensitivity of reverse-time migration with internal multiples: Geophysical Prospecting, **61**, 891–906.

Guitton, A., B. Kaelin, and B. Biondi, 2007, Least-squares attenuation of reverse-time-migration artifacts: Geophysics, **72**, S19–S23.

Holvik, E., and L. Amundsen, 2005, Elimination of the overburden response from multicomponent source and receiver seismic data, with source designature and decomposition into PP-, PS-, SP-, and SS-wave responses: Geophysics, **70**, S43–S59.

Ikelle, L. T., 2006, A construct of internal multiples from surface data only: the concept of virtual seismic events: Geophysical Journal International, **164**, 383–393.

Jakubowicz, H., 1998, Wave equation prediction and removal of interbed multiples: SEG Technical Program Expanded Abstracts 1988, Society of Exploration Geophysicists, 1527–1530.

Jiang, Z., J. Yu, G. T. Schuster, and B. E. Hornby, 2005, Migration of multiples: The Leading Edge, **24**, 315–318.

Kuo, J. T., and T. Dai, 1984, Kirchhoff elastic wave migration for the case of noncoincident source and receiver: Geophysics, **49**, 1223–1238.

Liu, Y., X. Chang, D. Jin, R. He, H. Sun, and Y. Zheng, 2011, Reverse time migration of multiples for subsalt imaging: Geophysics, **76**, WB209–WB216.

Majdański, M., C. Kostov, E. Kragh, I. Moore, M. Thompson, and J. Mispel, 2011, Attenuation of free-surface multiples by up/down deconvolution for marine towed-streamer data: Geophysics, **76**, V129–V138.

Malcolm, A. E., M. V. de Hoop, and H. Calandra, 2007, Identification of image artifacts from internal multiples: Geophysics, **72**, S123–S132.

Malcolm, A. E., B. r. Ursin, and M. V. de Hoop, 2009, Seismic imaging and illumination with internal multiples: Geophysical Journal International, **176**, 847–864.

Meles, G. A., K. Löer, M. Ravasi, A. Curtis, and C. A. da Costa Filho, 2014, Internal multiple prediction and removal using Marchenko autofocusing and seismic interferometry: Geophysics, **80**, A7–A11.

Minato, S., T. Matsuoka, T. Tsuji, D. Draganov, J. Hunziker, and K. Wapenaar, 2011, Seismic interferometry using multidimensional deconvolution and crosscorrelation for cross-well seismic reflection data without borehole sources: Geophysics, **76**, SA19–SA34.

Nemeth, T., C. Wu, and G. T. Schuster, 1999, Leastsquares migration of incomplete reflection data: Geophysics, **64**, 208–221.

Pica, A., and L. Delmas, 2008, Wave equation based internal multiple modeling in 3D: SEG Technical Program Expanded Abstracts, 2476–2480.

Ravasi, M., and A. Curtis, 2013, Elastic imaging with exact wavefield extrapolation for application to ocean-bottom 4C seismic data: Geophysics, **78**, S265–S284.

Reiter, E. C., M. N. Toksöz, T. H. Keho, and G. M. Purdy, 1991, Imaging with deepwater multiples: Geophysics, **56**, 1081–1086.

Reshef, M., S. Arad, and E. Landa, 2006, 3D prediction of surface-related and interbed multiples: Geophysics, **71**, V1–V6.

Rose, J. H., 2001, "Single-sided" focusing of the time-dependent Schrödinger equation: Physical Review A, **65**, 0127071–0127076.

———, 2002, Single-sided autofocusing of sound in layered materials: Inverse Problems, **18**, 1923–1934.

Sava, P., and S. Fomel, 2001, 3-D traveltime computation using Huygens wavefront tracing: Geophysics, **66**, 883–889.

Schneider, W. A., 1978, Integral Formulation for Migration in Two and Three Dimensions: Geophysics, **43**, 49–76.

Singh, S., R. Snieder, J. Behura, J. van der Neut, K. Wapenaar, and E. Slob, 2014, Autofocusing imaging: Imaging with primaries, internal multiples and free-surface multiples: SEG Technical Program Expanded Abstracts 2014.

———, 2015, Marchenko imaging: Imaging with primaries, internal multiples and free-surface multiples: Geophysics, **80**.

Slob, E., K. Wapenaar, F. Broggini, and R. Snieder, 2014, Seismic reflector imaging using internal multiples with Marchenko-type equations: Geophysics, **79**, S63–S76.

Stoffa, P. L., J. T. Fokkema, R. M. de Luna Freire, and W. P. Kessinger, 1990, Splitstep Fourier migration: Geophysics, **55**, 410–421.

Thorbecke, J., J. V. D. Neut, and K. Wapenaar, 2013, Green's function retrieval with Marchenko equations : a sensitivity analysis: SEG Technical Program Expanded Abstracts 2013, 3888–3893.

van der Neut, J., J. Thorbecke, K. Mehta, E. Slob, and K. Wapenaar, 2011, Controlled-source interferometric redatuming by crosscorrelation and multidimensional deconvolution in elastic media: Geophysics, **76**, SA63–SA76.

Verschuur, D. J., 1991, Surface-related multiple elimination, an inversion approach: Phd, Delft University of Technology.

———, 1992, Adaptive surface-related multiple elimination: Geophysics, **57**, 1166.

Vidale, J., 1988, Finite-difference calculation of travel times: Bulletin of the Seismological Society of America, **78**, 2062–2076.

Virieux, J., 1984, SH-wave propagation in heterogeneous media: Velocity-stress finite-difference method: Geophysics, **49**, 1933–1942.

———, 1986, P-SV wave propagation in heterogeneous media: Velocity-stress finite-difference method: Geophysics, **51**, 889–901.

Wapenaar, C. P. A., and G. C. Haimé, 1990, Elastic Extrapolation of Primary Seismic P- and S-waves: Geophys. Prospect., **38**, 23–60.

Wapenaar, C. P. A., N. Kinneging, and A. Berkhout, 1987, Principle of prestack migration

based on the full elastic two-way wave equation: Geophysics, **52**, 151–173.

Wapenaar, K., 2014, Single-sided Marchenko focusing of compressional and shear waves: Physical Review E, **90**, 063202.

Wapenaar, K., F. Broggini, E. Slob, and R. Snieder, 2013, Three-Dimensional Single-Sided Marchenko Inverse Scattering, Data-Driven Focusing, Green's Function Retrieval, and their Mutual Relations: Physical Review Letters, **110**, 084301.

Wapenaar, K., F. Broggini, and R. Snieder, 2012, Creating a virtual source inside a medium from reflection data: heuristic derivation and stationary-phase analysis: Geophysical Journal International, **190**, 1020–1024.

Wapenaar, K., and J. Fokkema, 2006, Green's function representations for seismic interferometry: Geophysics, **71**, SI33–SI46.

Wapenaar, K., and E. Slob, 2014, On the Marchenko equation for multicomponent single-sided reflection data: Geophysical Journal International, **199**, 1367–1371.

———, 2015, Initial conditions for elastodynamic Greens function retrieval by the Marchenko method: Presented at the SEG Technical Program Expanded Abstracts 2015.

Wapenaar, K., E. Slob, and R. Snieder, 2008, Seismic and electromagnetic controlled-source interferometry in dissipative media: Geophysical Prospecting, **56**, 419–434.

Wapenaar, K., J. Thorbecke, J. van der Neut, F. Broggini, E. Slob, and R. Snieder, 2014, Marchenko imaging: Geophysics, **79**, WA39–WA57.

Weglein, A. B., F. A. Gasparotto, P. M. Carvalho, and R. H. Stolt, 1997, An inverse-scattering series method for attenuating multiples in seismic reflection data: Geophysics, **62**, 1975–1989.

Yan, J., and P. Sava, 2008, Isotropic angle-domain elastic reverse-time migration: Geophysics, **73**, S229–S239.

Youn, O. K., and H. Zhou, 2001, Depth imaging with multiples: Geophysics, **66**, 246–255.

Ziolkowski, A., D. B. Taylor, and R. G. K. Johnston, 1999, Marine seismic wavefield measurement to remove sea-surface multiples: Geophysical Prospecting, **47**, 841–870.

Zuberi, M. A. H., and T. Alkhalifah, 2014, Generalized internal multiple imaging (GIMI) using Feynman-like diagrams: Geophysical Journal International, **197**, 1582–1592.

LIST OF FIGURES

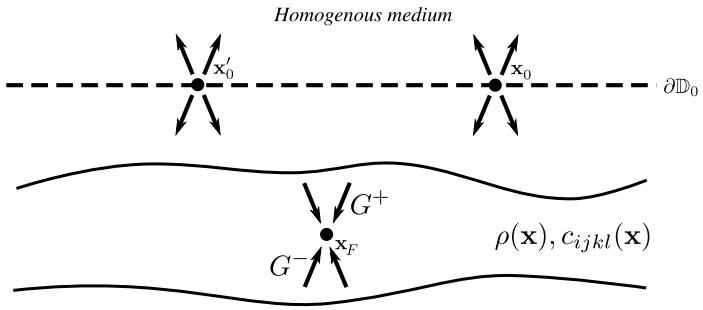

Figure 1: Conceptual solid-Earth model used herein. The boundary $\partial\mathbb{D}_0$ is transparent and represents the Earth's surface, separating the true subsurface from a homogenous medium above it. Surface sources (and receivers) are represented by $\mathbf{x}_0'$ and $\mathbf{x}_0$, with the arrows representing the direction of propagation of their Green's functions. The focus point $\mathbf{x}_F$ is in the subsurface and the arrows around it show the direction of the up- (G^-) and down-going (G^+) Green's functions that arrive there.

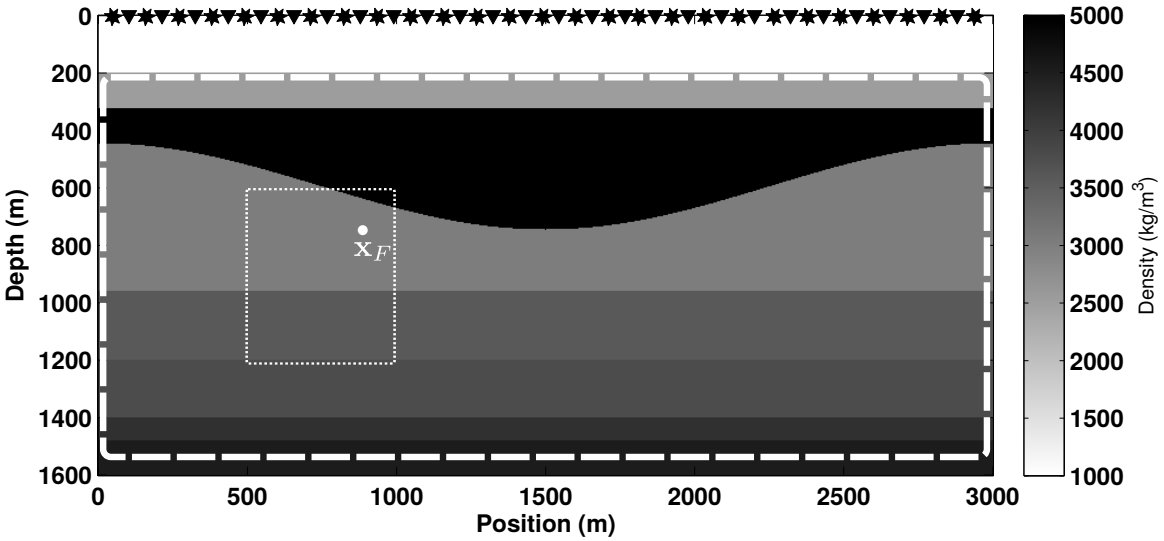

Figure 2: Density model and acquisition geometry. Sources (stars) and receivers (triangles) are collocated on the surface. The large dashed box indicates the area that will be imaged using single-component imaging conditions $I^{MM,ii}_{\mathrm{RI},v}$, $I^{MM,ii}_{\mathrm{AI},v}$ and $I^{MM,ii}_{\mathrm{dAI},v}$. The dotted box indicates the area that will be used for imaging using the tensorial imaging conditions $I^{MM,ii}_{\mathrm{RI},\tau}$, $I^{NN,ii}_{\mathrm{AI},\tau}$ and $I^{MM,ii}_{\mathrm{dAI},\tau}$.

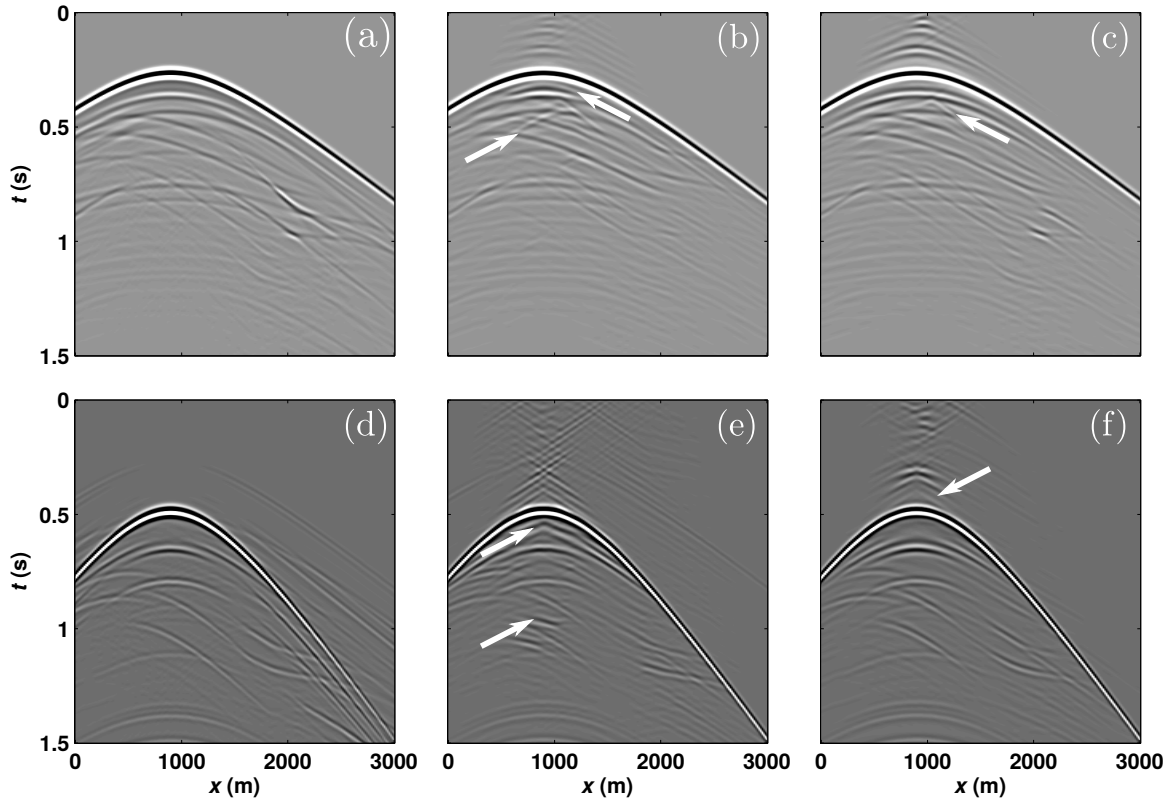

Figure 3: v_z components of the Green's functions from a subsurface P-wave source at point $\mathbf{x}_F$ shown in Figure 2 from (a) direct modeling, (b) elastic single-component autofocusing and (c) fully tensorial elastic autofocusing. v_x components of the Green's function from a subsurface S-wave source at point $\mathbf{x}_F$ from (d) direct modeling, (e) elastic single-component autofocusing and (f) fully tensorial elastic autofocusing. White arrows indicate nonphysical arrivals. For single-component autofocusing, 5 iterations were performed, for tensorial autofocusing, 3 iterations were performed. More iterations help to suppress acausal artifacts.

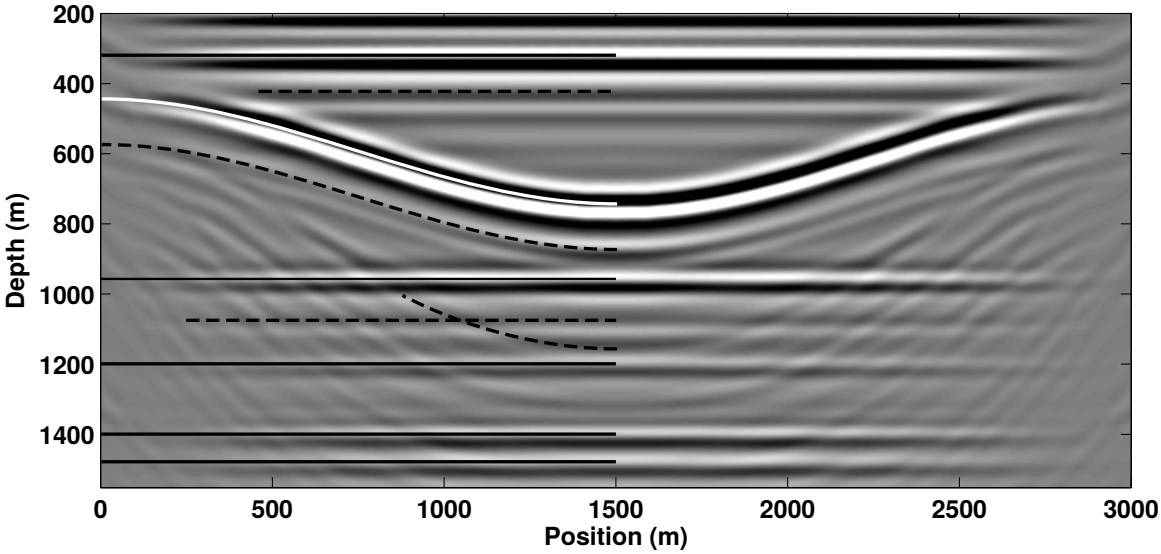

Figure 4: Reference PP image $I^{PP,zz}_{\mathrm{RI},v}$ from v_z recordings. Solid black and white curves indicate (the left half of) true reflector positions and dashed lines indicate spurious reflectors.

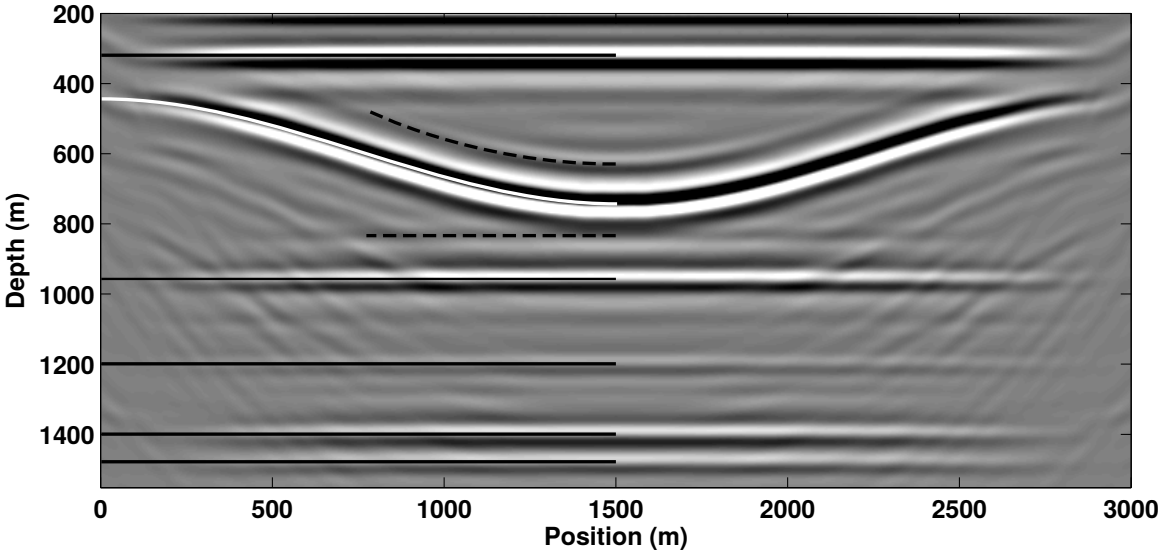

Figure 5: Autofocus PP image $I^{PP,zz}_{\mathrm{AI},v}$ from v_z recordings. Key as in Figure 4.

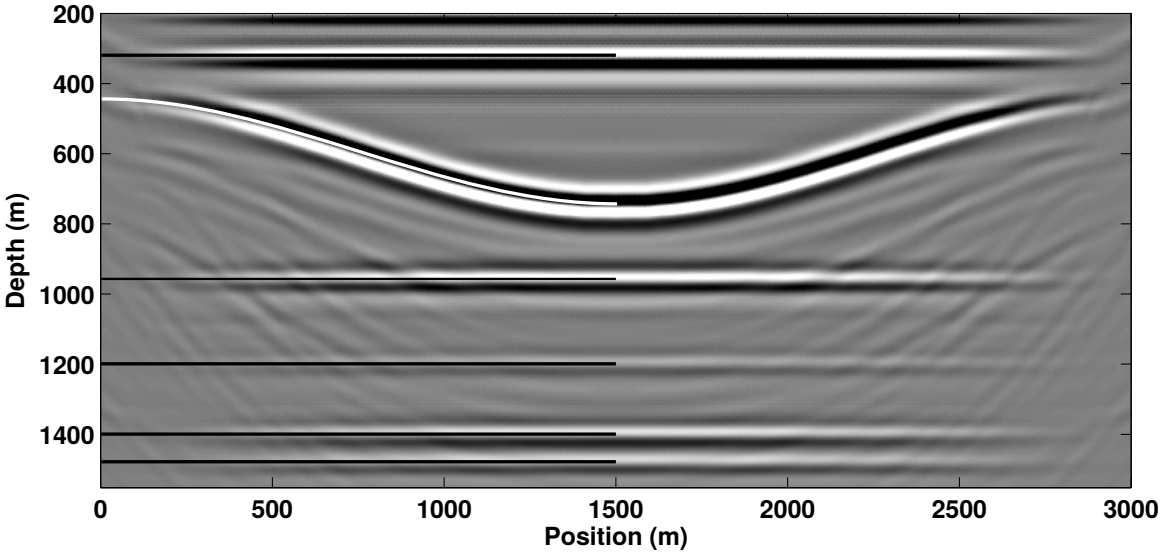

Figure 6: Direct-wave autofocus PP image $I^{PP,zz}_{\mathrm{dAI},v}$ from v_z recordings. Key as in Figure 4.

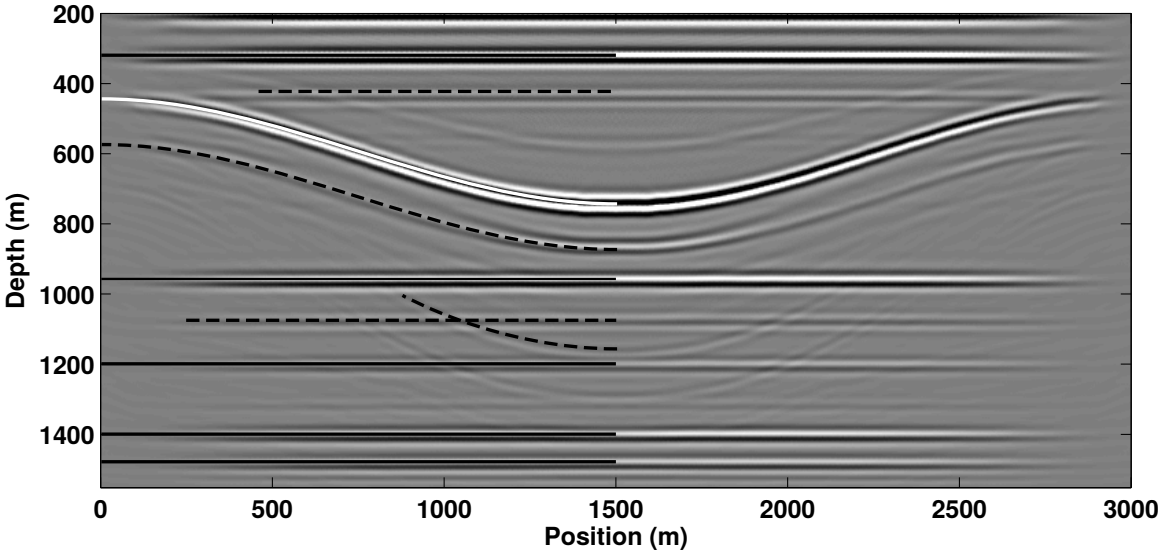

Figure 7: Reference SS image $I^{SS,xx}_{\mathrm{RI},v}$ from v_x recordings. Key as in Figure 4.

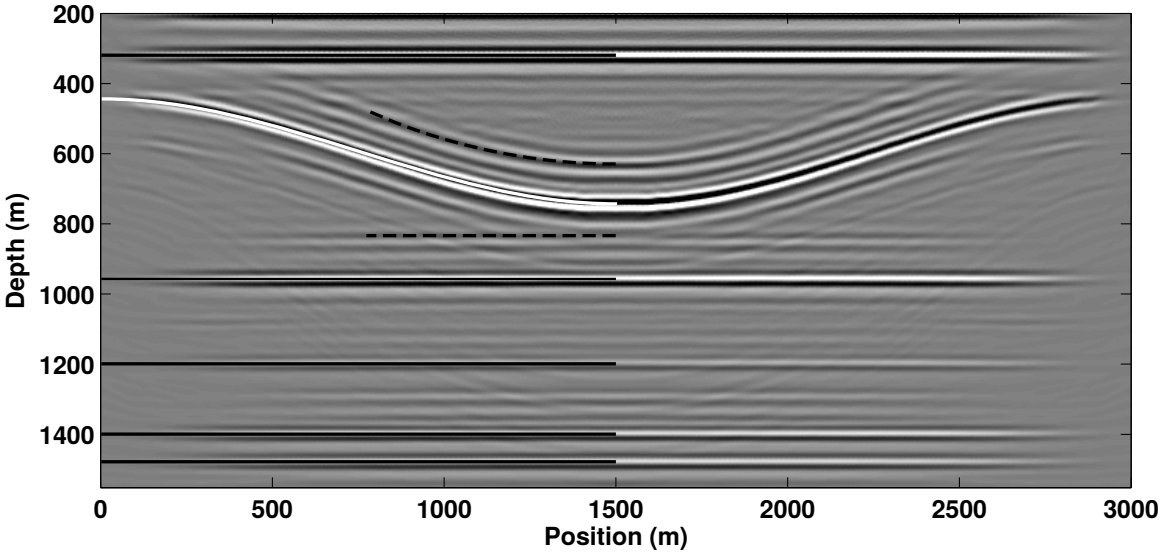

Figure 8: Autofocus SS image $I^{SS,xx}_{\mathrm{AI},v}$ from v_x recordings. Key as in Figure 4.

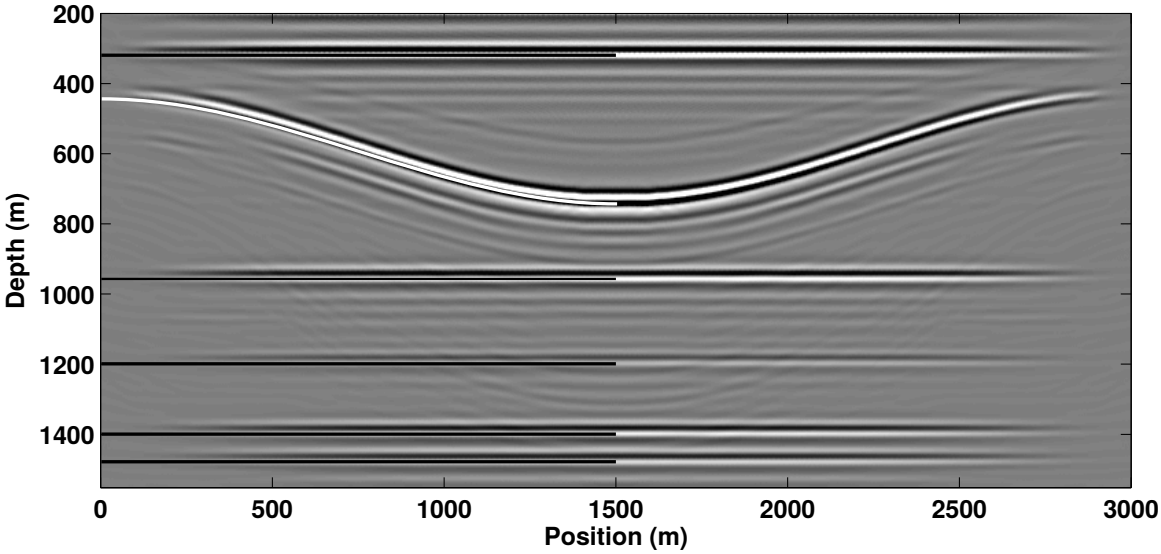

Figure 9: Direct-wave autofocus SS image $I^{SS,xx}_{\mathrm{dAI},v}$ from v_x recordings. Key as in Figure 4.

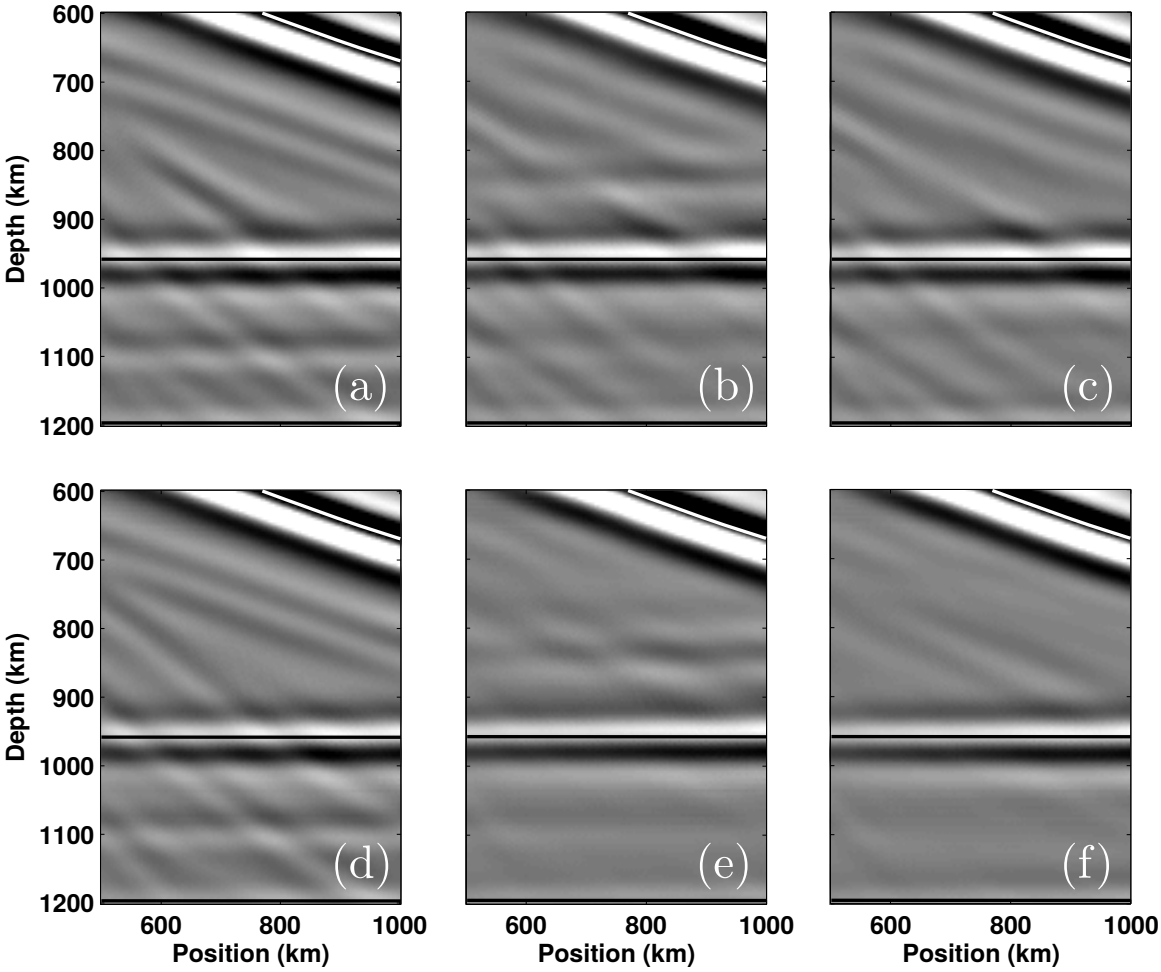

Figure 10: PP image details from the area enclosed by the white dotted box in Figure 2. Single-component (a) reference imaging $I^{PP,zz}_{\mathrm{RI},v}$, (b) autofocus imaging $I^{PP,zz}_{\mathrm{AI},v}$ and (c) direct-wave autofocus imaging $I^{PP,zz}_{\mathrm{dAI},v}$. Tensorial (d) reference imaging $I^{PP,zz}_{\mathrm{RI},\tau}$, (e) autofocus imaging $I^{PP,zz}_{\mathrm{AI},\tau}$ and (f) direct-wave autofocus imaging $I^{PP,zz}_{\mathrm{dAI},\tau}$. Key as in Figure 4.

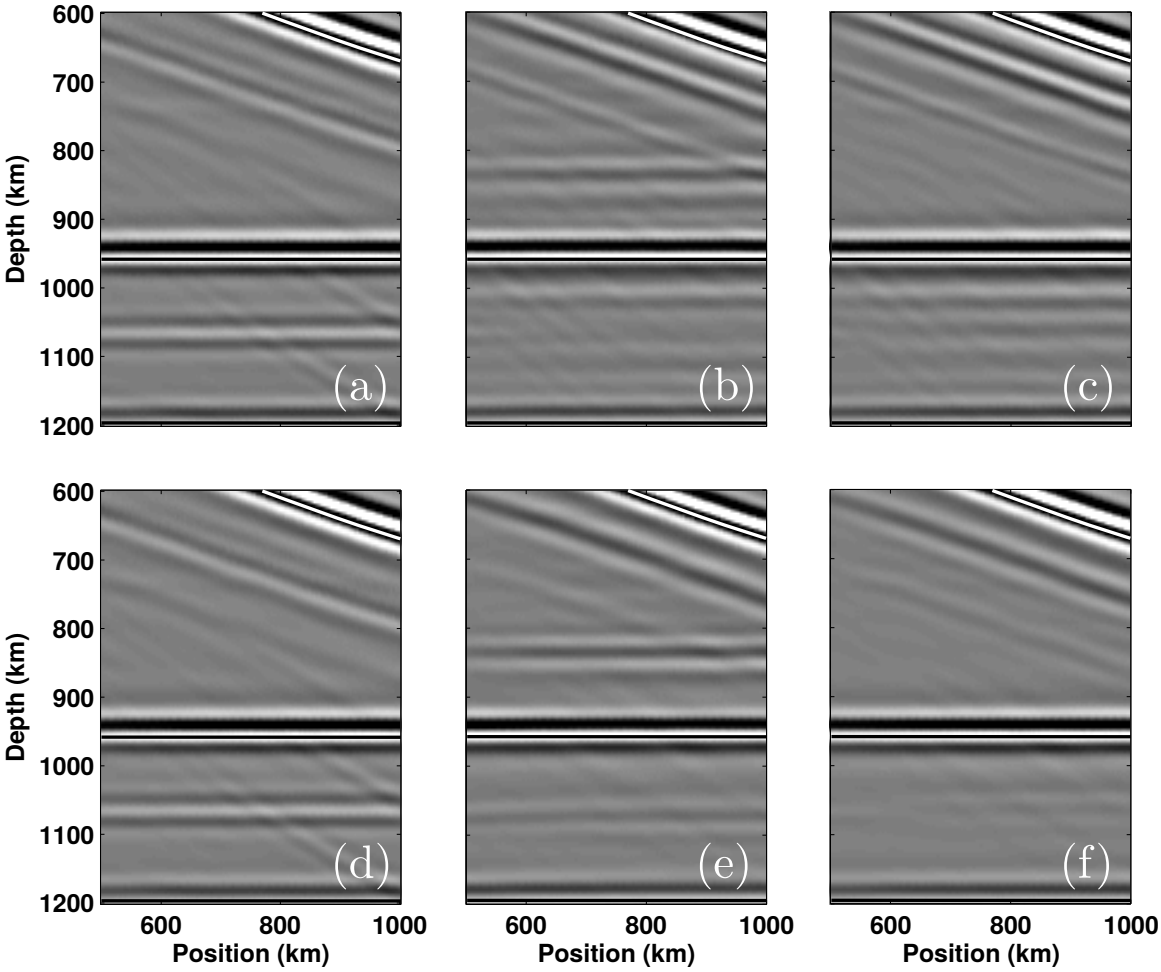

Figure 11: SS image details from the area enclosed by the white dotted box in Figure 2. Single-component (a) reference imaging $I^{SS,xx}_{\mathrm{RI},v}$, (b) autofocus imaging $I^{SS,xx}_{\mathrm{AI},v}$ and (c) direct-wave autofocus imaging $I^{SS,xx}_{\mathrm{dAI},v}$. Tensorial (d) reference imaging $I^{SS,xx}_{\mathrm{RI},\tau}$, (e) autofocus imaging $I^{SS,xx}_{\mathrm{AI},\tau}$ and (f) direct-wave autofocus imaging $I^{SS,xx}_{\mathrm{dAI},\tau}$. Key as in Figure 4.

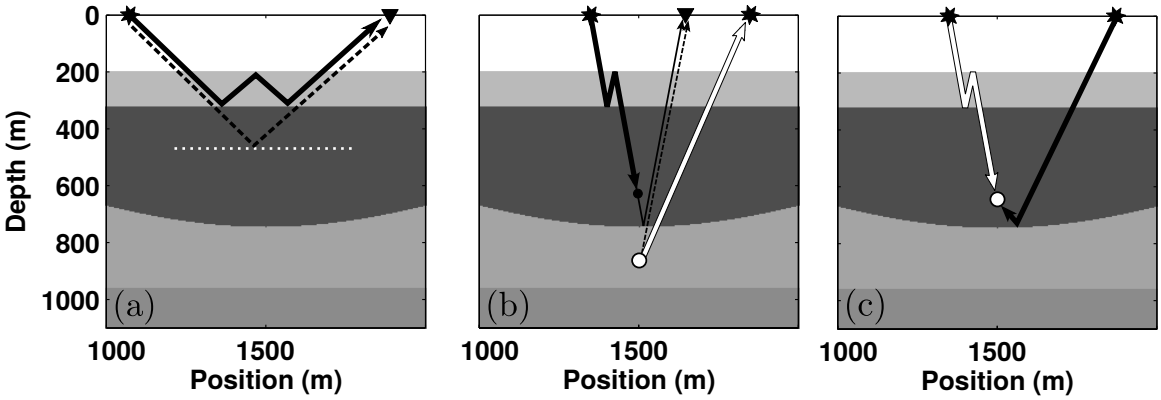

Figure 12: (a) Internal multiple reflection that resembles a primary in the reference imaging. The solid lines represent the raypath of the true internal multiple, and the dashed black lines represents the raypath of a primary that would have the same traveltime; the white dotted line indicates the ghost reflector in Figures 4 and 7. (b) Events that intersect to generate spurious reflectors under the second (counting from top to bottom) dashed curve in the reference images in Figures 4 and 7. (c) Events that intersect to generate spurious reflectors under the dashed curve in the autofocus images in Figures 5 and 8. White circles are image points; the black circle in (b) is a nonphysical apparent scattering point.